Atmos. Chem. Phys., 25, 8185–8211, 2025
https://doi.org/10.5194/acp-25-8185-2025

Atmospheric Chemistry and Physics
Open Access
EGU

Advances in characterization of black carbon particles and their associated coatings using the soot-particle aerosol mass spectrometer in Singapore, a complex city environment

Mutian Ma[1,a], Laura-Hélèna Rivellini[2], Yichen Zong[3,4], Markus Kraft[4,5], Liya E. Yu[1,2], and Alex King Yin Lee[6]

[1]Department of Civil and Environmental Engineering, National University of Singapore, Singapore
[2]NUS Environmental Research Institute, National University of Singapore, Singapore
[3]Department of Mechanical Engineering, National University of Singapore, Singapore
[4]Cambridge Centre of Advance Research and Education in Singapore, Singapore
[5]Department of Chemical Engineering and Biotechnology, University of Cambridge, Cambridge, United Kingdom
[6]Air Quality Processes Research Section, Environment and Climate Change Canada, ON, Toronto, Canada
[a]now at: Cambridge Centre of Advance Research and Education in Singapore, Singapore

Correspondence: Alex King Yin Lee (alex.lee@ec.gc.ca)

Received: 22 October 2024 – Discussion started: 11 November 2024
Revised: 19 May 2025 – Accepted: 22 May 2025 – Published: 30 July 2025

Abstract. Atmospheric black carbon can act as a short-lived climate forcer and carrier of toxic compounds. This work aims to utilize aerosol compositions detected by a soot-particle aerosol mass spectrometer to advance our understanding of the emission and atmospheric processing of refractory BC (rBC) in Singapore. Positive matrix factorization (PMF) analysis of rBC and organic aerosols (OAs) (PMF_{base}) identified two traffic factors with differences in rBC content, coating thickness, and diurnal pattern, which could potentially help differentiate gasoline and diesel vehicular emissions. Additionally, two secondary OA (SOA) factors influenced by local chemistry and/or regional transport (less-oxidized oxygenated OA (LO-OOA) and more-oxidized OA (MO-OOA)) were identified. Including metals in the PMF (PMF_{metal}) improved the quality of source apportionment significantly. An industrial- and shipping-influenced OA separated from traffic emissions was strongly associated with heavy metals (e.g., V^+ and Ni^+) that might pose higher potential risks to human health. Two biomass burning OA (BBOA) factors with different degrees of oxygenation were also identified. Although the aged BBOA component was highly oxidized, its strong association with $K_3SO_4^-$ distinguished it from other background MO-OOAs, which generally lacked distinctive OA signatures. Integration of both metals and inorganic aerosols (IAs) into the PMF (PMF_{all}) further identified an additional aged BBOA component that was associated with nighttime IAs and organo-nitrate formation. Furthermore, PMF_{all} revealed concurrent LO-OOA and nitrate formation during daytime, whereas photochemical production of MO-OOAs was linked to acidic sulfate formation, indicating the importance of investigating the interaction between SOA and IA formation and their mixing state in complex city environments.

Published by Copernicus Publications on behalf of the European Geosciences Union.

1 Introduction

Atmospheric black carbon (BC) particles generated by incomplete combustion of fossil fuel and biomass can have significant impacts on climate and human health. BC particles play a crucial role in radiative forcing, primarily through their ability to absorb sunlight (Bond et al., 2013). When deposited on snow and ice surfaces, BC particles reduce their albedo, accelerating melting and amplifying the effects of climate change (Bond et al., 2013). BC particles are always co-emitted with other particulate matter (PM), and atmospheric processing can lead to the formation of secondary PM that can subsequently condense onto the BC particles' surface (Bond et al., 2013; China et al., 2013; Collier et al., 2018; Lee et al., 2017). Coating formation on BC particles can modify their morphology, light absorbing properties, and chemical interaction with other atmospheric species – and hence their environmental fate and impacts (Cappa et al., 2019; China et al., 2013; Fierce et al., 2016; Kuwata et al., 2009; Peng et al., 2016; Wu et al., 2018). Furthermore, BC particles can co-emit and internally mix with toxic contaminants such as heavy metals and polycyclic hydrocarbon (PAH) from combustion processes (Corbin et al., 2018; Wang et al., 2021) and thus pose significant risks to human and ecosystem health.

Both primary and secondary organic aerosols (POAs and SOAs) have been found to be the major components of BC coatings based on soot-particle aerosol mass spectrometer (SP-AMS) measurements (Bibi et al., 2021; Cao et al., 2022; Collier et al., 2018; Farley et al., 2024; Lee et al., 2017; Wang et al., 2020; Willis et al., 2016), as the laser vaporization mode of SP-AMS allows detection of refractory BC (rBC, an operationally defined BC detected by SP-AMS) and their coating materials exclusively (Onasch et al., 2012). Although previous studies report different fullerene rBC fragment characteristics to differentiate burning sources (Bibi et al., 2021; Onasch et al., 2015; Wang et al., 2016), the interpretation of positive matrix factorization (PMF) solutions for distinguishing specific rBC-containing particle sources based on the mass spectral characteristics of rBC and organic aerosol (OA) coatings remains challenging. The mass spectral profiles of POAs emitted from various fossil fuel combustion sources are generally similar to each other and largely contributed by hydrocarbon ($C_xH_y^+$) fragments without distinctive differences (Carbone et al., 2019; Corbin et al., 2018; Dallmann et al., 2014; Ma et al., 2023). Furthermore, identifying the origins of highly oxidized/aged OA coatings is difficult because substantial atmospheric oxidative aging always diminishes the mass spectral features of POAs and leads to SOA products that are mainly dominated by a single OA fragment (i.e., CO_2^+), as illustrated in the observational frameworks developed based on the ambient AMS measurements worldwide (Cubison et al., 2011; Ng et al., 2010).

Previous studies have shown that the laser vaporization mode of SP-AMS can detect metals in both laboratory-generated and ambient rBC particles as well as engine emissions (Bibi et al., 2021; Cao et al., 2022; Carbone et al., 2015; Corbin et al., 2018; Dallmann et al., 2014; Rivellini et al., 2020; Tehrani et al., 2023). Given the higher stability of trace metals compared to OA (Lee et al., 2017) and the strong association of metals with combustion-related emissions, such unique measurement capability of SP-AMS has been used to obtain additional chemical information for improving the source identification of ambient rBC and OA particles and understanding the emission characteristics of specific combustion processes. For example, Bibi et al. (2021) clearly identified strong associations between different trace metals, in particular strontium (Sr), and fireworks when multiple primary emission sources were observed by SP-AMS during bonfire events (the Bonfire Night 2014 in Manchester, UK). Saarikoski et al. (2016) detected 15 trace metals in bus emissions that were dominated by rBC and OAs, and the relationships between the metals and rBC (e.g., vanadium (V) and zinc (Zn)) were different for acceleration and steady driving based on their SP-AMS observations. Corbin et al. (2018) investigated trace metals in heavy-fuel-oil combustion in a marine engine using an SP-AMS and demonstrated that vanadium-to-nickel (V/Ni) ratios in soot were much higher than those observed in $PM_{2.5}$ regardless of the engine loads. Cao et al. (2022) observed relatively high iron (Fe) signals on rBC particles in an urban area and hypothesized that Fenton chemistry might catalyze the observed formation of more oxidized SOAs. A few studies have shown that potassium (K) measured by SP-AMS could be used to indicate the potential influences of biomass burning emissions on rBC and OA particles in different urban and rural environments (Farley et al., 2023; Lee et al., 2016; Rivellini et al., 2020; Wang et al., 2017).

Singapore is a highly developed coastal urban environment located at the southern tip of the Malay Peninsula in Southeast Asia. In addition to typical local emissions from vehicular traffic and cooking (Budisulistiorini et al., 2018; Rivellini et al., 2020), Singapore hosts the world's second-busiest shipping port (World Shipping Council, 2024) and fifth-largest oil refining capacity (Lau et al., 2021), both of which are potentially significant anthropogenic sources of combustion-related PM and toxic pollutants to impact the local air quality. Moreover, air quality and concentrations of atmospheric PM in Singapore can be significantly influenced by SOAs (Budisulistiorini et al., 2018; Rivellini et al., 2020) and transboundary haze caused by biomass burning emissions transported from surrounding regions in Southeast Asia (Budisulistiorini et al., 2018; Heil and Goldammer, 2001; Kuwata, 2024). Given the unique capability of the SP-AMS to simultaneously detect rBC particles and their associated coatings, this study explores multiple PMF scenarios based on SP-AMS measurements, iteratively incorporating rBC, OAs, inorganic aerosols (IAs), and metals into the input. This step-by-step PMF interpretation approach underscores the value of including all measured chemical species

in the analysis to better resolve local primary emissions and the secondary transformation processes of rBC-containing particles in Singapore. The improved characterization presented in this study provides important insights into how industrial emissions may introduce toxic heavy metals and influence local SOA formation in a complex urban environment. It also sheds light on how regional biomass burning may affect background levels of rBC-containing particles in Southeast Asia's urban atmosphere.

2 Methodology

2.1 Sampling site and collocated measurements

The measurements were conducted from 28 January to 17 March 2022 at the E2 building on the campus of the National University of Singapore (1°18′ N, 103°46′ E; 67 m above sea level). Figure 1 shows the sampling site location and details of the surrounding environment. The air quality at the site can be significantly influenced by anthropogenic emissions, as reported in our previous work (Rivellini et al., 2020). The measurement site was located south of the AYE highway and northeast of multiple shipping ports and industrial regions with refineries and petrochemical plants. An SP-AMS (Aerodyne Research) was deployed to measure the chemical composition of submicron rBC-containing particles (see Sect. 2.2 for details of the SP-AMS measurements). Co-located BC mass concentration was measured using a seven-wavelength Aethalometer (AE33, Magee Scientific) (Drinovec et al., 2015; Hansen et al., 1984), and non-refractory PM_1 (NR-PM_1) was measured by a time-of-flight aerosol chemical speciation monitor (ToF-ACSM, Aerodyne Research; see detailed description in the Supplement; Fröhlich et al., 2013). The SP-AMS, ToF-ACSM, and Aethalometer shared a Teflon-coated cyclone inlet with a cutoff size of 2.5 µm (model 2000-30ED, URG), and the aerosol stream was dried by a Nafion™ dryer system (Aerodyne Research). Gas-phase species (NO_x and O_3) were measured by a low-cost sensor system (AQMesh air quality measurement system, Environmental Instruments Ltd., UK). Meteorological parameters were measured, including wind speed and direction (03001 RM Young Wind Sentry Set, Campbell Scientific Inc.), solar radiation (LI-COR model LI-200X, Campbell Scientific Inc.), rainfall (Hydro-logical Services CS700, Campbell Scientific Inc.), relative humidity (RH), and temperature (AQMesh air quality measurement system, Environmental Instruments Ltd., UK).

2.2 Soot-particle aerosol mass spectrometer (SP-AMS)

SP-AMS is a standard high-resolution time-of-flight aerosol mass spectrometer (HR-ToF-AMS, Aerodyne Research) equipped with a laser vaporizer (LV). In this work, the SP-AMS was configured to detect rBC-containing particles (rBC is an operationally defined term that refers to the BC particles detected by SP-AMS) and their associated coating materials, including organic (Org), nitrate (NO_3^-), sulfate (SO_4^{2-}), chloride (Cl^-), ammonium (NH_4^+), and trace metals in PM_1 (Carbone et al., 2015; Corbin et al., 2018; Lee et al., 2017). The resistively heated tungsten vaporizer (TV) of the SP-AMS was removed for this study so that non-rBC-containing particles, which are not vaporized by the LV, were not detected. In contrast, the ToF-ACSM only has a TV for aerosol vaporization and thus detects total NR-PM_1 components (i.e., Org, NO_3^-, SO_4^{2-}, Cl^-, and NH_4^+) regardless of their aerosol mixing state with rBC. The comparison of SP-AMS and ToF-ACSM measurements can provide quantitative information on the degree of mixing between rBC and NR-PM_1 (Lee et al., 2017; Wang et al., 2017; Xu et al., 2018; Yu et al., 2020).

The working principle of LV and the detailed description of SP-AMS have been reported by Onasch et al. (2012). In brief, particles are focused by an aerodynamic lens with an effective detection range between 70 and 1000 nm in diameter. rBC-containing particles are heated up to ∼4000 K and vaporized by the 1064 nm continuous Nd-YAG intra-cavity infrared (IR) laser module. At such high temperatures, refractory coating materials (such as metals and certain inorganic salts) can also be vaporized. The vapors are subsequently ionized by the 70 eV electron impact and then detected by a high-resolution time-of-flight mass spectrometer operated in V-mode with a mass spectral resolving power of ∼2000 at m/z 28 (Canagaratna et al., 2007; DeCarlo et al., 2006). The particle vacuum aerodynamic diameter (d_{va}) is measured by the efficient particle time-of-flight (ePToF) system. The SP-AMS samples at a 1 min interval for measuring bulk aerosol mass spectra and size distributions, followed by a 2 min interval for event trigger single particle (ETSP) measurement. The ETSP data are not reported in this work.

2.3 SP-AMS calibration

Regal Black (Regal 400R pigment black, Cabot Corp.) was used to calibrate the mass-based ionization efficiency of rBC (mIE_{rBC}) for SP-AMS without the TV. Regal Black particles were first suspended in ultrapure water (Milli-Q, 18.2 MΩ cm (25 °C) and total organic carbon (TOC) < 5 ppb). The suspension was sonicated continuously during atomization by a constant output atomizer (model 3076, TSI Inc.). The droplets were then dried by a diffusion dryer and the dried particles were size-selected at 300 nm using a differential mobility analyzer (DMA, model 3081, TSI Inc.) for the SP-AMS calibration. The sum of carbon ion clusters from C_1^+ to C_{10}^+ was used to quantify rBC mass for both ambient and calibration data. Due to the significant interferences from OAs, the average C_1^+-to-C_3^+ ratio of 0.66 obtained from the Regal Black calibration was used to determine C_1^+ signals from rBC in ambient aerosol. Three sets of calibrations were performed throughout the sampling period.

Monodispersed and dried ammonium nitrate (NH_4NO_3) particles at 300 nm were generated using the atomization

Figure 1. Sampling location (red star) and surrounding environment. The yellow lines indicate the major roadways. A large industrial area with petrochemical industries and shipping ports is located south of the sampling location (source: © Google Earth 2024).

method described above to determine the mass-based ionization efficiency of NO_3^- (mIE_{NO_3}). However, because pure NH_4NO_3 particles cannot be vaporized by the LV scheme, direct determination of mIE_{NO_3} was not possible for SP-AMS without TV. Therefore, mIE_{NO_3} and mIE_{rBC} were first determined for our SP-AMS using the dual vaporization (DV, i.e., both TV and LV were installed) configuration. Note that mIE_{NO_3} and mIE_{rBC} were determined when the LV was off and on, respectively. The TV was operated at 600 °C throughout the calibration. A relative ionization efficiency of rBC ($RIE_{rBC} = mIE_{rBC}/mIE_{NO3}$) of 0.24 was then obtained. Assuming that RIE_{rBC} does not change with the TV configuration, mIE_{NO_3} for the SP-AMS without TV can be calculated accordingly (i.e., $mIE_{NO_3} = mIE_{rBC}/0.24$). The calculated mIE_{NO_3} and the default RIE values of NO_3^- (1.1), SO_4^{2-} (1.2), Cl^- (1.3), Org (1.4), and NH_4^+ (4.0) (Jimenez et al., 2003) were used to quantify those NR-PM_1 coated on the rBC core (referred to as NR-$PM_{coating}$ hereafter). We note that previous studies have suggested that this calibration approach may overestimate the mass of NR-$PM_{coating}$ (Lee et al., 2015; Willis et al., 2014). Given the potential contribution by organo-nitrates (see Sect. 3.5.2), the mass concentrations of inorganic nitrate likely represent their upper limit.

Trace metals coated on the rBC core can be detected by the LV configuration of SP-AMS (Carbone et al., 2015; Corbin et al., 2018; Rivellini et al., 2020). In this work, five metal-related ions, i.e., sodium (Na^+), potassium (K^+), rubidium (Rb^+), vanadium (V^+), and nickel (Ni^+), were detected by the SP-AMS, with their signals higher than the limit of detection during most of the sampling period (see Table S1 in the Supplement). In addition, $K_3SO_4^+$ ions (m/z 213) originating from potassium sulfate were also observed and will be discussed with the five metal-related ions. The signals of these six ions were not calibrated, and hence they are not included in the mass concentrations of NR-$PM_{coating}$ reported in this study. The raw signals (Hz) of these metal ions were used for most of the data analysis except for the source apportionment of OAs and rBC, which is based on positive matrix factorization (PMF) analysis of fragment ions detected by the SP-AMS (see Sect. 2.5 for details).

2.4 SP-AMS data processing

The SP-AMS measurement was processed by the AMS data analysis software SQUIRREL, version 1.65C, for unit mass resolution data and by PIKA, version 1.35C, for high-resolution peak fitting (Sueper, 2015). The daily particle-free ambient air was collected for determining the instrument lower detection limit and for correcting the fragmentation table to reduce interferences due to the air (Allan et al., 2004; DeCarlo et al., 2006). Elemental ratios of OA coatings were determined using the Improved-Ambient method (Canagaratna et al., 2015) with the conversion factor applied for oxygen-to-carbon (O : C) and hydrogen-to-carbon (H , C) ratios for LV measurements (Ma et al., 2021). The carbon oxidation state of OA (OS_c) was calculated based on the O : C and H : C ratios (i.e., $OS_c \approx 2 \cdot O:C - H:C$) (Kroll et al., 2011). The collection efficiency (CE) for rBC particles is largely governed by the overlapping between the particle beam and laser beam (Willis et al., 2014), depending on the particle shape. Willis et al. (2014) reported a CE value of 0.6 for bare BC, but CE can increase with the coating mass (i.e., NR-PM coating mass / rBC mass ratio, R_{BC}, greater than 1).

The average R_{BC} value for this study was 0.44 ± 0.24, and hence a constant CE value of 0.6 was applied in this work.

2.5 PMF analysis of SP-AMS data

PMF analysis has been widely used to identify various sources of ambient OAs measured by aerosol mass spectrometers (Ulbrich et al., 2009; Zhang et al., 2011). In this work, the PMF evaluation tool (PET, v3.05D Ulbrich et al., 2009) was used to identify potential sources and characteristics of rBC particles and their associated coatings. The OA and rBC (C_n^+) fragments were included for performing PMF analysis to form the base case in this work (PMF_{base-n}, where n represents the number of factors in the PMF solution selected for discussion). Similar to typical PMF analysis of OA fragments alone, ions with a signal-to-noise ratio (SNR) between 0.2 and 2.0 were downweighted by a factor of 2. CO_2^+-related ions (i.e., O^+, HO^+, H_2O^+, and CO^+) and C_1^+ were also downweighted. Ions with SNR < 0.2 were removed from the analysis. This version of PMF analysis has been used in previous studies to better resolve combustion sources at different locations (Carbone et al., 2019; Lee et al., 2017; Massoli et al., 2015; Rivellini et al., 2020; Wang et al., 2017).

Given that metal ions are relatively inert in response to the chemical aging of atmospheric aerosol, integrating metal ions in PMF may better resolve the origin and emission characteristics of rBC-containing particles in complex urban environments. The metal-related ions (i.e., Na^+, K^+, Rb^+, V^+, Ni^+, and $K_3SO_4^+$) were included in our PMF analysis (denoted as $PMF_{metal-n}$ hereafter). Due to the large uncertainties of RIE for metals, the PMF_{metal} results would only be used for identifying potential origins of OAs, and the metal concentrations were not included in the total mass concentration of each PMF factor. The signals of K^+, Rb^+, V^+, and Ni^+ were either downweighted or upweighted to produce SNRs comparable to those of typical OA and rBC fragments. For instance, strong fragments such as $C_2H_3O^+$ and C_3^+ exhibit SNRs of ~ 25 and ~ 21, respectively. To bring K^+ into a comparable range, its signal was downweighted by a factor of 10, resulting in an SNR of ~ 13. In contrast, the signals of Rb^+, V^+, and Ni^+ were each upweighted by a factor of 3 to achieve SNRs of ~ 6. Figure S1 in the Supplement demonstrates how adjusting the SNR of K^+ improves the performance of PMF as an example. Previous studies of SP-AMS measurements have also used a similar approach to integrate metal-related ions into PMF analysis (Bibi et al., 2021; Carbone et al., 2015; Rivellini et al., 2020). To further investigate the nature and formation of OAs, IA-related fragments from sulfate, nitrate, and chloride were included in the PMF analysis. This PMF analysis included all the measured aerosol components (i.e., OA + rBC + metal + IA) (denoted as PMF_{all-n} hereafter). Sulfate ions that exhibited SNRs between 10 and 30 were downweighted by a factor of 3. Nitrate ions and $K_3SO_4^+$ had SNR values in the range of 5 to 15 that do not require adjustment. Note that downweighted and upweighted signals of AMS data for PMF analysis have been more systematically investigated by previous studies to improve the separation of factors (Lee and Hopke, 2006; Paatero and Hopke, 2003; Reff et al., 2007).

An RIE value of 1 was used for all the species applied in the PMF analysis, and their mass concentrations were determined using their RIE values for each factor described in Sect. 2.3. The PMF results were evaluated for up to 10 factors, with FPEAK values between -1 and 1 and a step change of 0.2. As noted below, the first 3 days of the sampling period had elevated concentrations of rBC-containing particles due to significant influences of regional transport. Removing this short period does not make significant changes in the PMF results. The $Q/Q_{expected}$ plots for different PMF scenarios up to the 10-factor solution are shown in Fig. S2. A detailed interpretation of the selected solution for each PMF input (i.e., PMF_{base-n}, $PMF_{metal-n}$, and PMF_{all-n}) will be discussed in Sect. 3.2–3.5. Factors from each solution will be denoted as "Factor name"$_{solution-n}$ (e.g., Factor-A identified in PMF_{base-4} will be referred to as Factor-A_{base-4}).

2.6 Wind and air mass back trajectory analysis

The potential sources of pollutants were estimated using ZeFir nonparametric wind regression (NWR), as described by Petit et al. (2017), using Igor Pro (Ver. 8.04, WaveMetrics Inc.). To achieve potential sources of pollutants, both high-resolution temporal wind information (i.e., wind speed and direction) and pollutant concentration are required to calculate nearby sources (Henry et al., 2009). In this study, the NWR graphs were generated for an angle resolution of 1° and a radial resolution of 0.1 m s^{-1} with program-suggested smooth parameters of 12 and 2.21, respectively. The origins of air masses were generated by the Hybrid Single-Particle Lagrangian Integrated Trajectory (HYSPLIT) model coupled with meteorological data from the Global Data Assimilation System (GDAS, 1°) for 5 d back for every hour. This model was developed by the National Oceanic and Atmospheric Administration (Draxler and Hess, 1998). Cluster analysis was also performed using the HYSPLIT model, with details given by previous studies (Baker, 2010; Borge et al., 2007). The potential source contribution function (PSCF) was used to analyze regional transport and sources to expand the source knowledge to a larger scale (Polissar et al., 2001). The PSCF model re-distributes pollutant concentration or hotspots based on the air mass trajectories' residence times. In this work, the PSCF model was set to consider the species concentration above their 75th percentile with a cell size of 0.1° and smoothing of 2.

3 Results and discussion

3.1 Measurements overview

Figure 2a–c presents the meteorological parameters (solar radiation, precipitation, RH, temperature, wind speed, and wind direction) during the measurement period. The average temperature and RH were 28 °C and 85 %, respectively, and reached their daily maximum (∼ 31 °C) and minimum (∼ 70 % RH) at ∼ 13:00 LT (Fig. 3a). The sampling period covered the northeast monsoon season, which is supported by the cluster analysis of the 72 h air mass back trajectory showing that regional transport of air mass from the region northeast of Singapore dominated the campaign period (Fig. S3), where multiple fires were observed (Fig. S4). No precipitation was observed for most of the sampling period, with only a few days having rainfall higher than 1 mm. In general, solar radiation was strong during daytime, which could lead to oxidized secondary coating formation on rBC particles (i.e., Org/rBC, R_{BC}, and O : C of organic coating peaked at ∼ 13:00 LT), as illustrated in Fig. 3b and c. The wind blew from the northwest for the majority of the sampling period and generally shifted to the southwest/southeast in the afternoon, where it could carry shipping and industrial emissions from the coastal area to the measurement site (Fig. 3d). Detailed NWR and PSCF analysis for individual species and PMF factors will be provided in Sect. 3.2–3.5 for identifying local emissions and regional transport of aerosol components.

The time series of chemical components of rBC-containing particles measured by the SP-AMS are shown in Fig. 2d–f. The average total mass concentration of rBC plus NR-$PM_{coating}$ was $6.37 \pm 4.15\,\mu g\,m^{-3}$. rBC was the major component ($4.47 \pm 2.89\,\mu g\,m^{-3}$), accounting for ∼ 70 wt % of rBC-containing particles. The main contributor of NR-$PM_{coating}$ was Org ($1.67 \pm 1.44\,\mu g\,m^{-3}$), which contributed to ∼ 26 wt % of the rBC-containing particles. The IA components ($SO_4^{2-} = 0.16 \pm 0.16\,\mu g\,m^{-3}$, $NO_3^- = 0.06 \pm 0.05\,\mu g\,m^{-3}$, $Cl^- = 0.02 \pm 0.01\,\mu g\,m^{-3}$, and $NH_4^+ = 0.02 \pm 0.01\,\mu g\,m^{-3}$) were minor contributors to the NR-$PM_{coating}$ mass (Fig. 2e). The rBC concentrations measured by the SP-AMS were about 31 % higher than the equivalent BC (eBC) concentrations measured by the Aethalometer. A strong temporal correlation between the two measurements was observed, suggesting that the temporal variation of BC concentrations can be captured reasonably well by both instruments ($R = 0.89$, Fig. S5). Such strong correlation between the eBC and rBC concentrations was consistently observed at the same sampling location (Rivellini et al., 2020). The descriptions of the size distributions of rBC, aerosol species, and OA fragments in NR-$PM_{coating}$ are reported in the Supplement. The average mass concentration of NR-PM_1 measured by ToF-ACSM was $15.05 \pm 8.68\,\mu g\,m^{-3}$ ($Org = 7.06 \pm 4.64\,\mu g\,m^{-3}$, $SO_4^{2-} = 6.16 \pm 4.29\,\mu g\,m^{-3}$, $NO_3^- = 0.55 \pm 0.57\,\mu g\,m^{-3}$, $NH_4^+ = 1.44 \pm 1.03\,\mu g\,m^{-3}$, and $Cl^- = 0.09 \pm 0.15\,\mu g\,m^{-3}$). The time series correlations of SP-AMS and ToF-ACSM for Org, SO_4^{2-}, NO_3^-, Cl^-, and NH_4^+ are shown in Fig. S5b–f. Figure S6 shows the time series and overall composition of NR-PM_1. Strong correlations were observed for all species ($R > 0.74$) except for ammonium ($R = 0.33$). Based on the SP-AMS and ToF-ACSM measurements (i.e., NR-$PM_{coating}$ vs. NR-PM_1), ∼ 16 % of OAs and less than 6 % of each IA component were coated on rBC particles (Fig. S5), suggesting that most of the NR-PM_1 materials were externally mixed with rBC in this study.

The correlation coefficients between all the species measured by the SP-AMS are reported in Fig. S7. As the major component of NR-$PM_{coating}$, Org had strong correlations with rBC ($R = 0.8$), implying that large fractions of coated Org are co-emitted primarily with rBC from various combustion sources. In contrast, SO_4^{2-}, NO_3^-, Cl^-, and NH_4^+ are only weakly or moderately correlated with rBC ($R = 0.32$–0.53), which is consistent with the fact that these IA components are generally secondarily formed in the atmosphere. A previous measurement in Singapore showed that SO_4^{2-} can be the second-largest NR-PM_1 contributor (∼ 38 % NR-PM_1 mass) (Rivellini et al., 2020), and we observed that rBC particles were not the major condensation sink for the secondary IA components (i.e., less than 5 %, Fig. S5). Regarding the metal-related ions, Na^+, K^+, and $K_3SO_4^+$ gave much stronger signals compared to V^+, Ni^+, and Rb^+ (Fig. 2f). Among all the detected metal-related ions, Na^+ had the strongest correlations with rBC ($R = 0.73$), followed by V^+ ($R = 0.58$) and Ni^+ ($R = 0.44$), whereas K^+, Rb^+, and $K_3SO_4^+$ were only weakly correlated with rBC ($R < 0.3$). The wide range of correlation coefficients between rBC and different metals suggests multiple combustion sources of rBC particles with different metal contents observed at the measurement site (see Sect. 3.2.1).

3.2 Characteristics of rBC and associated coating materials

3.2.1 Characteristics of metal ions associated with rBC-containing particles

Figure 4a shows that the mass loadings of rBC remained low at night and increased during the morning and evening rush hours (08:00–09:00 and 20:00 LT), indicating that local traffic is one of the key contributors to rBC. Furthermore, rBC concentrations started increasing at ∼ 12:00 LT and peaked at 17:00–18:00 LT along with Org, SO_4^{2-}, NO_3^-, Na^+, Ni^+, and V^+. The afternoon peak of these species could be partially due to the wind from the south (Fig. 3d), which could carry emissions from shipping ports and/or the industrial region to the measurement site occasionally (Fig. 1) (Betha et al., 2013; Budisulistiorini et al., 2018; Jaafar et al., 2018; Rivellini et al., 2020). A distinct hotspot was observed south of our measurement site for Na^+, V^+, and Ni^+ under relatively

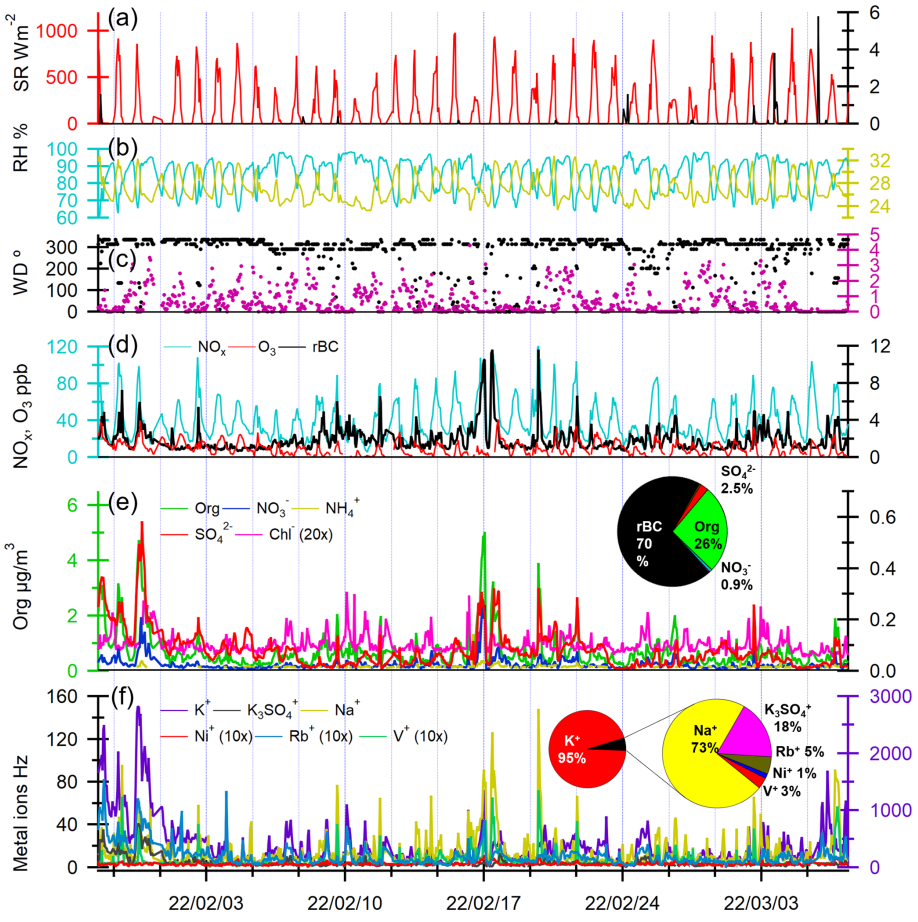

Figure 2. Time series of **(a)** solar radiation (SR) and precipitation, **(b)** RH and temperature, **(c)** wind direction and wind speed, **(d)** NO_x, O_3, and rBC concentrations, **(e)** Org, SO_4^{2-}, NO_3^-, Cl^-, and NH_4^+ concentrations, and **(f)** metal-related ion intensities. The pie charts in panels **(e)** and **(f)** show the overall mass distribution of rBC and NR-$PM_{coating}$ in rBC-containing particles and the metal-related ion signal distribution (Hz) in rBC-containing particles, respectively.

high wind speed conditions ($> 8\,m\,s^{-1}$, Fig. 4g–i), and their concentrations were not significantly influenced by regional transport, as shown in their PSCF plots (Fig. 5). Assuming a similar RIE for V^+ and Ni^+, the average V^+/Ni^+ ratios at the afternoon peak were approximately equal to 4–5 (with the 75th percentile > 6, Fig. 6a). These observations suggest that these metal ions can be used to indicate the impacts of shipping and/or industrial emissions on specific rBC and OA sources identified in the PMF analysis (see Sect. 3.3).

A strong correlation was observed between K^+ and Rb^+ ($R = 0.75$, Fig. S7), and they had relatively high concentrations at midnight (Fig. 4j and k). Although potassium and rubidium are not unique tracers for a specific combustion source, our previous SP-AMS measurements with the DV scheme at the same site reported a strong temporal correlation between these two ions and highlighted that K^+ and Rb^+ can be used to understand the impacts of regional biomass burning on aged background SOAs (Rivellini et al., 2020). $K_3SO_4^+$ is strongly correlated with K^+ ($R = 0.83$, Fig. S7) in this work. Detectable signals of $K_3SO_4^+$ indicate the presence of potassium sulfate (K_2SO_4). Potassium salts generated from biomass burning are typically in the form of potassium chloride (KCl), which can react with acid gases (e.g., H_2SO_4 and HNO_3) heterogeneously to form K_2SO_4 and potassium nitrate (KNO_3) during the aging process (Li et al., 2003, 2010). Previous SP-AMS measurements have reported the detection of $K_3SO_4^+$ in rBC-containing particles in Beijing and the Tibetan Plateau and have used $K_3SO_4^+$ as an indicator for aged or transported biomass burning organic aerosol (BBOA) (Wang et al., 2020). In addition to SP-AMS measurements, Murphy and Thomson (1997) were able to detect $K_3SO_4^+$ from plume that contained biomass burning pollution using positive ion laser ionization single particle analysis. K_2SO_4 has also been detected as potassium ion clusters, including $K_3SO_4^+$ and $K_2HSO_4^+$, in aged biomass burning particles by the positive mode of aerosol time-of-flight mass spectrometers (ATOFMS) (Zauscher et al., 2013).

The PSCF analysis and NWR plots show that the elevated signals for K^+, Rb^+, and $K_3SO_4^+$ are associated with the regional transport of air masses from north of Singapore

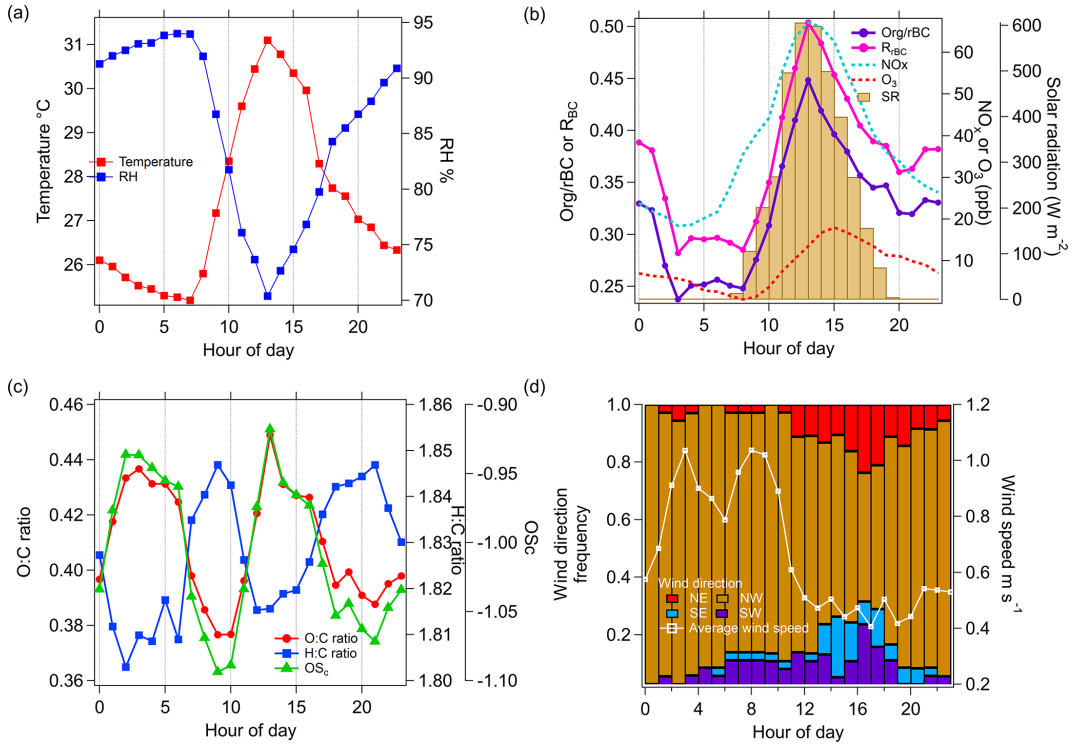

Figure 3. Diurnal cycles of **(a)** temperature and RH, **(b)** Org/rBC ratio, R_{BC}, NO_x, O_3, and solar radiation (SR), **(c)** O : C, H : C, and OS_c of organic coatings on rBC particles, and **(d)** wind direction fraction distribution and wind speed.

(Figs. 4 and 5), indicating the potential large influence of regional biomass burning emissions with different degrees of aging on the chemical composition of NR-$PM_{coating}$, and the high intensities were mainly observed at the beginning of our study period (29–31 January 2022, Fig. 2f). Figure S4 shows the regional fire events observed during 22–29 January 2022. Furthermore, the diurnal cycle of the $K_3SO_4^+/K^+$ ratio illustrates additional sources of $K_3SO_4^+$ in the afternoon compared to K^+ (i.e., heterogeneous conversion of background potassium salts to K_2SO_4). Overall, the above observations suggest that K^+, Rb^+, and $K_3SO_4^+$ can be potentially useful to indicate the relative importance of fresh and aged biomass burning emissions on specific rBC and OA sources identified in the PMF analysis (see Sect. 3.3).

3.2.2 Characteristics of OA components in NR-$PM_{coating}$

OA was the major component of NR-$PM_{coating}$, accounting for ~ 26 wt % of the rBC-containing particles. The organic-to-rBC (Org/rBC) ratio and elemental ratios (i.e., O : C, H : C, and OS_c) are useful parameters for identifying the nature of OA coating (e.g., POAs vs. SOAs). As shown in Fig. 3b and c, the diurnal patterns of Org/rBC, O : C, and OS_c have lower values, indicative of POAs, at 08:00–09:00 and 20:00–21:00 LT, during which the local traffic emissions are the primary sources of rBC (see Sect. 3.2.1). The Org/rBC, O : C, and OS_c started increasing significantly at 10:00 LT, and their peaks were observed at 12:00–13:00 LT, when the solar radiation was the strongest. This observation suggests that condensation of photochemically produced SOAs can lead to a notable increase in OA coating thickness, although most of the OAs in NR-PM_1 were externally mixed with rBC particles (see Sect. 3.1).

The Org/rBC ratio declined in the afternoon and then remained roughly the same between 18:00 and 02:00 LT the next day. The higher O : C ratio and OS_c overnight suggests an increasing contribution of oxidized organic species to the total OA coatings, which is consistent with the greater influence from regional transport of aged aerosols with biomass burning influences overnight, as discussed above in Sect. 3.2.1. To investigate the possible biomass burning influences on OA coatings, a mass contribution of a biomass burning tracer fragment to the total organic coating ($f_{C_2H_4O_2^+}$) was determined, as shown in Fig. 6d. Cubison et al. (2011) reported that $f_{C_2H_4O_2^+} > 0.3$ % obtained from standard AMS measurements can be an indication of biomass burning influences. Ma et al. (2021) showed that $f_{C_2H_4O_2^+}$ can be enhanced by a factor of ~ 2.45 on average for oxygenated organic coating and 2.33 for levoglucosan vaporized by the LV scheme of SP-AMS. Therefore, the background level of $f_{C_2H_4O_2^+}$ was recalculated using the correction factor of 2.33, as shown by the dashed horizontal line in Fig. 6d. Although the $f_{C_2H_4O_2^+}$

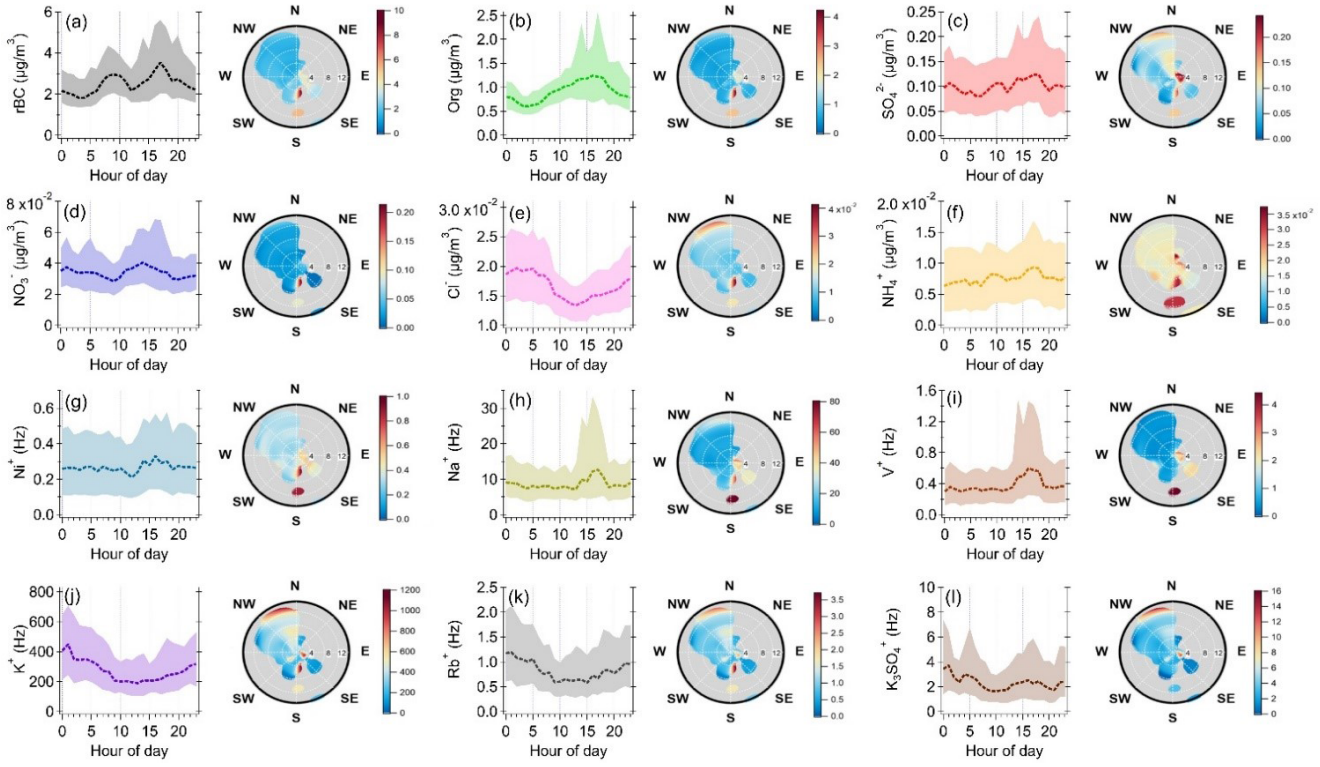

Figure 4. Diurnal cycles and NWR plots of individual species measured by SP-AMS: median (dashed line) and 25th and 75th percentiles (shaded areas). Mass concentrations of organic and inorganic species are corrected by CE and RIE, except for metal ions and $K_3SO_4^+$, which are shown in terms of signal intensity (Hz). The wind speed unit in the NWR plots (radial axis) is $m\,s^{-1}$. The color scale of the NWR plots represents the species concentration or signal intensity ($\mu g\,m^{-3}$ or Hz).

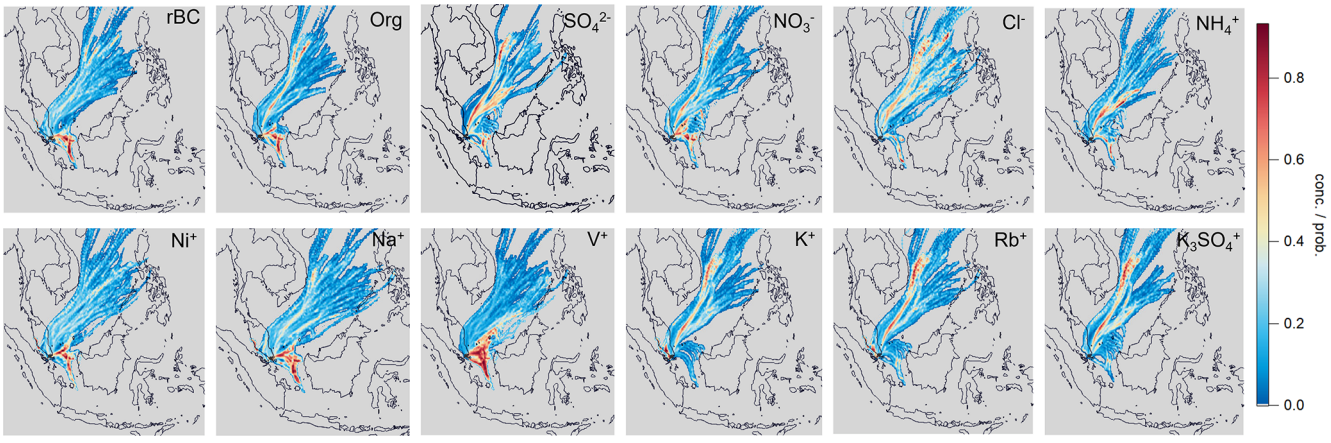

Figure 5. PSCF plots for individual species measured by SP-AMS. The PSCF model was set to consider the species concentration above their 75th percentile.

values of total OAs were close to the background level, the higher values of $f_{C_2H_4O_2^+}$ and OS_c of OA coating materials between 02:00 and 08:00 LT suggests potential influences of biomass burning emissions on the chemical characteristics of rBC-containing particles during the night. The potential contribution of fresh and aged biomass burning emissions will be further discussed based on the PMF analysis (see Sect. 3.3).

3.2.3 Characteristics of IA components in NR-$PM_{coating}$

Although NO_3^-, SO_4^{2-}, Cl^-, and NH_4^+ together accounted for less than 4 wt % of the rBC-containing particles (Fig. 2e),

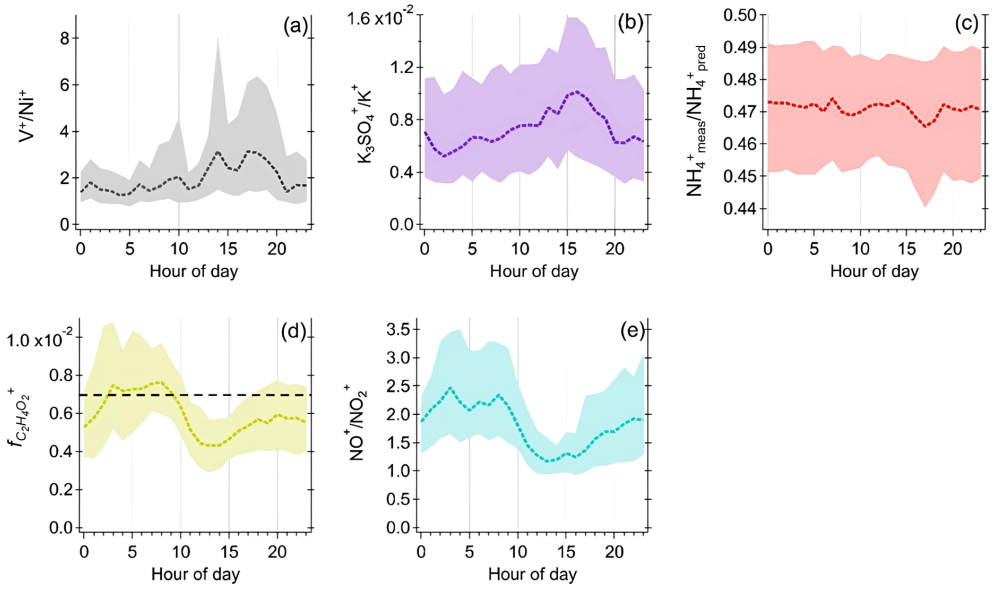

Figure 6. Diurnal cycles of **(a)** V^+/Ni^+, **(b)** $K_3SO_4^+/K^+$, **(c)** $NH_{4\,meas}^+/NH_{4\,pred}^+$, **(d)** $f_{C_2H_4O_2^+}$, and **(e)** NO^+/NO_2^+ measured by SP-AMS. The horizontal dashed line in **(d)** represents the background level of $f_{C_2H_4O_2^+}$ for non-BBOA reported by Cubison et al. (2011), with the correction factor for OAs measured by the LV scheme applied (Ma et al., 2021).

their temporal variations can still be useful for evaluating the potential sources of rBC-containing particles and the atmospheric processes that the particles might have experienced. The elevated concentrations of SO_4^{2-} and NO_3^- together with rBC and a few metal ions between 14:00 and 19:00 LT (Fig. 4) suggest potential impacts of the atmospheric processing of shipping and/or industry emissions on SO_4^{2-} and NO_3^- concentrations (Sect. 3.2.1). The average $NH_{4\,meas}^+ / NH_{4\,pred}^+$ (Zhang et al., 2007) was ~0.47 most of the time, implying that acidic aerosols were locally formed via photooxidation and subsequently condensed on rBC particles and that they could not be completely neutralized by gas-phase ammonia before they reached the site. The ionic balance of NR-PM_1 from the ACSM measurements also shows that the average $NH_{4\,meas}^+ / NH_{4\,pred}^+$ (~0.6) is consistent with a previous standard AMS measurement in Singapore (Rivellini et al., 2020), further supporting the overall acidic aerosols. A similar observation has been reported for NR-PM_1 based on the SP-AMS measurement with the DV scheme at the same site (Rivellini et al., 2020). The SO_4^{2-} concentration is the highest, followed by the NO_3^- and Cl^- concentrations (38 % and 13 % of the SO_4^{2-} concentration, respectively), so SO_4^{2-} is likely the major component affecting the aerosol acidity. The oxidation of biogenic dimethyl sulfide (DMS) from the ocean can produce methanesulfonic acid (MSA) that might contribute to the detected sulfate-related fragments at our sampling site (Rivellini et al., 2020), but the signature peaks of MSA and organosulfur compounds, including CH_3SO^+, $CH_2SO_2^+$, and $CH_3SO_2^+$ (Farmer et al., 2010; Ge et al., 2012; Rivellini et al., 2020; Saarikoski et al., 2019), were not detected in this work.

It is important to point out that the NO^+/NO_2^+ ratio (i.e., the two major fragments for quantifying NO_3^-) has been widely used to determine the presence of organo-nitrate based on the standard AMS measurement, as the ratios of organo-nitrate are generally higher than those of inorganic nitrate (Farmer et al., 2010; Ng et al., 2017; Xu et al., 2015). Configuring the SP-AMS with the LV scheme alone, the average NO^+/NO_2^+ ratio for NH_4NO_3 coated on Regal Black particles generated in the laboratory is ~0.9. The higher NO^+/NO_2^+ ratios (~2–3.6) between 19:00 and 11:00 LT (Fig. 6e) suggest the existence of organo-nitrate in this work. On the contrary, the lower NO^+/NO_2^+ ratio during daytime suggests that photochemical production of inorganic nitrate was more important than that of organo-nitrate. The large similarity between the diurnal patterns of $f_{C_2H_4O_2^+}$ (Fig. 6d) and the NO^+/NO_2^+ ratio (Fig. 6e) indicates that biomass burning aerosol can be a possible contributor of organo-nitrate during the sampling period (Lin et al., 2016, 2017). Organo-nitrate can be produced via nocturnal NO_3 radical and N_2O_5 chemistry (Fry et al., 2018). A laboratory study has shown that under higher RH condition (50 % vs. 10 %), NO_3 radicals formed from the dark reaction of O_3 and NO_2 can promote up to 70 % more SOA mass formation with BBOAs (Kodros et al., 2020), suggesting that aged BBOAs can be a significant secondary source for organo-nitrate through nighttime chemistry.

3.3 Source apportionment of rBC and OA coatings based on PMF_{base}

In this section, source apportionment analysis of rBC and OA coatings is presented, and the PMF_{base-4} results are considered as a base case for comparison in the later sections. Figure 7 shows mass spectra, diurnal cycles, and time series of the PMF_{base-4} solution determined by the OA and rBC fragments. The major types of particles identified in the PMF_{base-4} were rBC-rich, hydrocarbon-like OA (HOA), less-oxidized oxygenated OA (LO-OOA), and more-oxidized oxygenated OA (MO-OOA) factors. The rBC-rich$_{base-4}$ factor is the major rBC contributor ($\sim$ 80%), while OA mass was more evenly distributed among the four factors, with the rBC-rich$_{base-4}$, HOA$_{base-4}$, LO-OOA$_{base-4}$, and MO-OOA$_{base-4}$ factors accounting for 17 %, 31 %, 21 %, and 31 % of the total OAs, respectively (Fig. 8).

3.3.1 POAs from fossil fuel combustion

The HOA$_{base-4}$ factor was dominated by aliphatic fragments ($C_xH^+_{2x-1}$ and $C_xH^+_{2x+1}$), with the highest mass contribution to OAs in NR-$PM_{coating}$ (31 %). The rBC fragments accounted for only $\sim$ 13.2 % of HOA$_{base-4}$ mass, resulting in an Org/rBC ratio of 6.6. The low O : C ratio of this factor (0.14) suggests the primary nature of the HOA coating. The rBC-rich$_{base-4}$ factor was dominated by C^+_1–C^+_5 fragments, with the highest mass contribution to total rBC (80 %). The rBC-rich$_{base-4}$ factor has a C^+_1/C^+_3 ratio of 0.67 that is similar to that of the Regal Black standard and in line with the range of rBC emitted from diesel engines or locomotive engines (Carbone et al., 2019; Corbin et al., 2014; Onasch et al., 2012). The CO^+ and CO^+_2 fragments accounted for 38 % of the OA mass in the rBC-rich$_{base-4}$ factor. These two oxygenated fragments can be due to the presence of oxidized organic compounds and soot functionality, and hence the mass and O : C ratio of the OA coating may be overestimated in the rBC-rich$_{base-4}$ factor. $C_3O^+_2$ is another oxygenated rBC fragment that has been observed in refractory soot structures of laboratory-generated diesel soot particles (Ma et al., 2023). The $C_3O^+_2/C^+_3$ signal (Hz) ratio observed in the rBC-rich$_{base-4}$ factor is 0.094. Assuming that all CO^+, CO^+_2, and $C_3O^+_2$ signals are from rBC, the Org/rBC ratio drops from 0.37 to $\sim$ 0.1 for rBC-rich$_{base-4}$. Therefore, the observation of lower Org/BC, O : C, and OS_c in Fig. 3 indicates that the rBC emitted from local traffic was mainly coated by POAs and that the thickness of such POA coatings was relatively thin for the majority of the rBC particles compared to those observed during the rest of the day. Assuming spherical-shaped particles, the rBC-rich particles are estimated to have a coating thickness contributing to 4.6 % of the overall particle diameter (see Supplement for coating thickness estimation and Table S2).

The HOA$_{base-4}$ and rBC-rich$_{base-4}$ factors had similar diurnal profiles (Fig. 7) and strongly correlated with the bulk rBC concentrations ($R = 0.99$ and 0.92, respectively), indicating that they represent rBC and POA components emitted from local combustion sources. Nevertheless, there are two major differences between the temporal variations of HOA$_{base-4}$ and rBC-rich$_{base-4}$ worth highlighting. Firstly, the diurnal profile of rBC-rich$_{base-4}$ peaked 1 hour earlier than that of HOA$_{base-4}$ during morning rush hours. This could be due to the relatively high contribution of heavy-duty diesel trucks to the total traffic volume in the early morning of Singapore (Fwa et al., 1996). This speculation is well-aligned with an on-road investigation using SP-AMS that heavy-duty diesel trucks emit much higher rBC content than gasoline vehicles, but the OA mass spectral features in emission plumes are similar between them (Dallmann et al., 2014). Secondly, outside of the rush hours, both factors started increasing at $\sim$ 12:00 LT and peaked at 17:00–18:00 LT, which coincided with prevailing wind blowing from the industrial and shipping region located to the south. The NWR plots show high concentrations of both HOA and rBC-rich factors at the hotspot observed from the south when the wind speed was greater than 8 m s^{-1}, but the HOA$_{base-4}$ concentrations exhibited a stronger enhancement at this hotspot than the rBC-rich$_{base-4}$ factors. Although most of the previous studies assigned their HOA and rBC-rich factors as local traffic-related OAs (Carbone et al., 2019; Gentner et al., 2017; Malmborg et al., 2017), our results suggest that rBC-rich$_{base-4}$ and HOA$_{base-4}$ can be emitted from multiple combustion sources. Nevertheless, the PMF_{base} could not further resolve the contributions of traffic and shipping/industrial emissions to these two primary OA factors.

3.3.2 SOAs from local chemistry and regional transport

Two secondary OA factors, namely, LO-OOA and MO-OOA, were identified by PMF_{base-4}. The mass spectra of LO-OOA$_{base-4}$ were dominated by a $C_2H_3O^+$ fragment, with comparable contributions between the other $C_xH^+_y$ and $C_xH_yO^+_z$ fragments. LO-OOA$_{base-4}$ had an O : C ratio of 0.51, which is more oxygenated than the HOA$_{base-4}$ factors. The diurnal profile of LO-OOA$_{base-4}$ increased during daytime together with solar radiation (Figs. 7 and 3b). The PSCF plot of LO-OOA$_{base-4}$ (Fig. 7) also suggests that the elevated concentrations of LO-OOA$_{base-4}$ were not strongly associated with regional transport of air mass. Given that rBC accounted for only 1.6 % of the mass of LO-OOA$_{base-4}$, the high Org/rBC ratio of LO-OOA$_{base-4}$ (61.0) suggests that the LO-OOA$_{base-4}$ factor likely represents freshly formed SOAs due to local photooxidation chemistry that are thickly coated on rBC particles within a relatively short timescale. Note that this hypothesis remains valid even though the Org/rBC ratios for LO-OOA reduce to $\sim$ 18 in the PMF_{metal} and PMF_{all} scenarios (see Sect. 3.4 and 3.5 and Table S3), which is still considered as thickly coated rBC-containing particles compared to other ambient observations (Cappa et

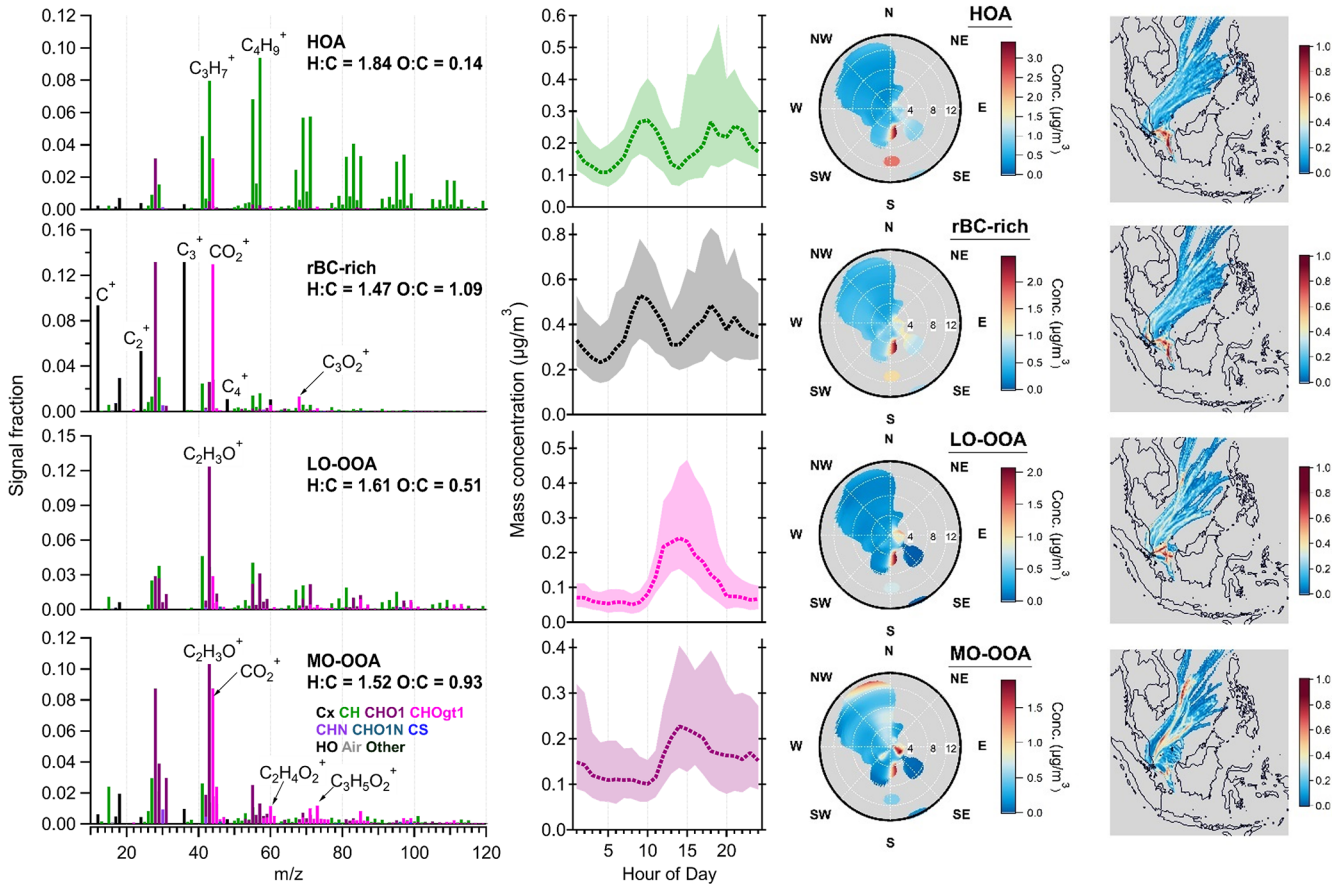

Figure 7. Results of PMF_{base-4} factors: mass spectra of OAs and rBC (first column), diurnal cycles of mass concentrations (second column, median: dashed lines, 25th/75th percentiles: shaded areas), NWR plots (third column), and PSCF plots (fourth column). The PMF mass spectra were not RIE-adjusted for different species. The wind speed unit in the NWR plots (radial axis) is $m\,s^{-1}$. The color scale of the NWR plots represents the species concentration ($\mu g\,m^{-3}$). Some of the NWR plots are presented with different wind speed ranges ($< 3\,m\,s^{-1}$) and resolutions in Fig. S8.

al., 2019) (see Supplement for coating thickness estimation and Table S2).

The mass spectra of $MO\text{-}OOA_{base-4}$ were dominated by the $C_2H_3O^+$ and CO_2^+ fragments. The $MO\text{-}OOA_{base-4}$ factor has an O : C ratio of 0.93, and hence $MO\text{-}OOA_{base-4}$ likely represents the more oxygenated SOA components compared to $LO\text{-}OOA_{base-4}$. rBC accounted for 12.8 % of the $MO\text{-}OOA_{base-4}$ mass, with an Org/rBC ratio of 6.8. Similar to $LO\text{-}OOA_{base-4}$, $MO\text{-}OOA_{base-4}$ increased during daytime with solar radiation (Figs. 7 and 3b), indicating the important contribution of local photochemistry to MO-OOA production. However, the PSCF plot of MO-OOA also highlighted the significant regional transported contribution, especially from the first 3 days of this field campaign (Fig. 7, i.e., the data shown in yellow and red for $MO\text{-}OOA_{base-4}$). The $MO\text{-}OOA_{base-4}$ factor has a much higher value of $f_{C_2H_4O_2^+}$ (1.2 %) than the threshold value of 0.3 % derived by Cubison et al. (2011). Nevertheless, the $f_{C_2H_4O_2^+}$ values of $MO\text{-}OOA_{base-4}$ reduced to ∼ 0.5 % when the conversion factor of 2.45 derived by Ma et al. (2021) was applied for more direct comparison with the standard AMS observation (TV scheme) reported by Cubison et al. (2011). In fact, $MO\text{-}OOA_{base-4}$ was strongly associated with $K_3SO_4^+$ ($R = 0.86$), K^+ ($R = 0.84$), and Rb^+ ($R = 0.68$) and gave similar hotspots in the PSCF plots, suggesting that the MO-OOA factor was likely influenced by the regional transport of biomass burning emissions (Figs. 7 and 5).

The PMF_{base-5} solution was investigated to explore whether BBOAs can be separated from the existing factors. PMF_{base-5} yields an additional OA factor, with a $f_{C_2H_4O_2^+}$ value of 1.6 % (denoted as $BBOA\text{-}HOA_{base-5}$ in Fig. S9). This new factor increased during nighttime and peaked at ∼ 01:00 LT. The result suggests that PMF_{base-5} attempts to separate the relatively fresh BBOA components from the total OAs, but the origin of this OA factor remains hard to interpret without additional information, as its mass spectrum was dominated by fragments similar to those observed in HOAs (i.e., $C_xH_y^+$; see HOA_{base-5} and $BBOA\text{-}HOA_{base-5}$

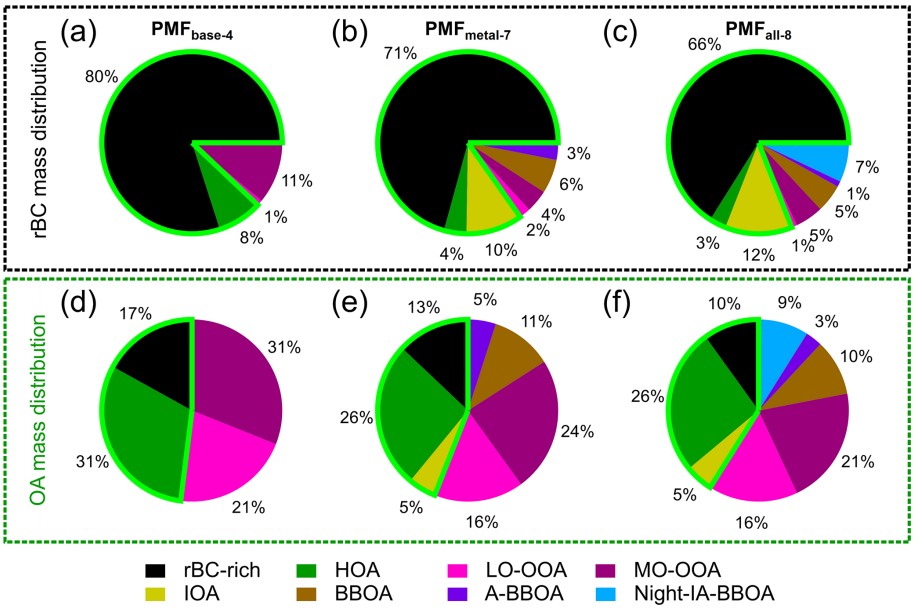

Figure 8. rBC **(a–c)** and Org **(d–f)** mass distributions for different PMF factors: PMF_{base-4} **(a, d)**, $PMF_{metal-7}$ **(b, e)**, and PMF_{all-8} **(c, f)**. The light-green boundary in each pie chart indicates the total contribution of PMF factors that are related to primary emissions from anthropogenic combustion.

in Fig. S9). Furthermore, the $f_{C_2H_4O_2^+}$ value of the MO-OOA_{base-5} factor remains high (1.0 %), indicating that a significant amount of the highly oxidized OA materials still cannot be separated from the relatively fresh BBOA components during the measurement period, as they might mix well in the regional air mass before reaching the measurement site.

3.4 Improved identification of industrial and biomass burning sources based on PMF_{metal}

The six metal-related ions (i.e., Na^+, K^+, Rb^+, V^+, Ni^+, and $K_3SO_4^+$) were integrated into the PMF analysis. PMF_{base-4} and $PMF_{metal-4}$ identify the same types of rBC-containing particles (i.e., rBC-rich, HOA, LO-OOA, and MO-OOA), and there are good correlations of mass spectra and temporal variations between the corresponding factors (i.e., the correlation coefficients between their mass spectra, $R_{m/z} > 0.98$, and time series, $R_{ts} > 0.94$, of PMF_{base-4} and $PMF_{metal-4}$, Table S4). This suggests that the addition of metal ions does not significantly affect the performance of PMF analysis in identifying the four major particle types. Figure 9 shows the distribution of the metal ions in each factor from $PMF_{metal-4}$. The majority of K^+, $K_3SO_4^+$, and Rb^+ signal intensities ($\sim$ 85 %) were associated with MO-$OOA_{metal-4}$, which provides evidence to support our hypothesis that the MO-OOA_{base-4} factor could be significantly influenced by regional transported biomass burning emissions (see Sect. 3.3.2). On the other hand, a significant portion of Na^+, Ni^+, and V^+ signals were apportioned to the $HOA_{metal-4}$ and rBC-$rich_{metal-4}$ factors, highlighting that these two primary factors could be impacted by combustion emissions from shipping and/or industry nearby, as previously discussed (see Sect. 3.2.1).

In this section, the higher number of PMF_{metal} solutions were investigated to improve our understanding of (1) the potential impacts of shipping/industrial emissions on the rBC-rich and HOA factors and (2) the contributions of biomass burning emissions to MO-OOAs due to the regional transport. The $PMF_{metal-7}$ is considered as the optimum solution in this work, with the details shown in Fig. 10. Three additional types of rBC-containing particles with reasonable physical meanings, namely, the industrial and shipping-related factor (IOA), aged BBOAs (A-BBOAs), and BBOAs, can be resolved by $PMF_{metal-7}$. The rBC-rich, HOA, LO-OOA, and MO-OOA factors identified by $PMF_{metal-7}$ were still the major contributors to rBC and OA masses (Fig. 8), and they gave similar mass spectra (i.e., rBC and OA fragments) and time series compared to those corresponding factors determined by $PMF_{metal-4}$ ($R_{m/z} > 0.84$ and $R_{ts} > 0.92$, Table S5), suggesting that the chemical characteristics and temporal variabilities of the four original factors were not significantly affected by the new factors.

3.4.1 Identification of rBC-containing particles from industrial emissions

The $IOA_{metal-7}$ factor likely represents primary combustion emissions. This factor is composed of 51 wt % of rBC and has organic mass spectra dominated by hydrocarbon fragments (i.e., $C_xH_y^+$). Unlike the rBC-$rich_{metal-7}$ and

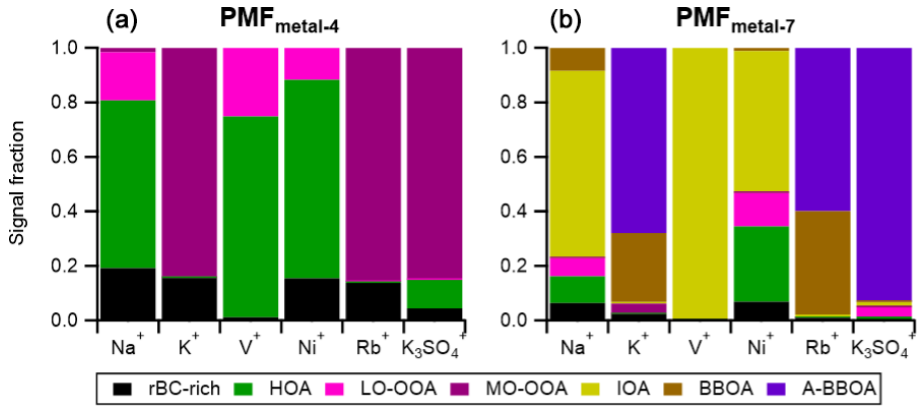

Figure 9. Metal signal contributions to individual factors identified by $PMF_{metal-4}$ **(a)** and $PMF_{metal-7}$ **(b)**.

$HOA_{metal-7}$ factors, $IOA_{metal-7}$ did not increase during the traffic rush hours (Fig. 10). The concentrations of $IOA_{metal-7}$ substantially increased between 15:00 and 20:00 LT, and the large difference between the median and 75th percentile of $IOA_{metal-7}$ concentrations during the peak period suggests that a very strong IOA emission was occasionally transported from the industrial region and shipping ports to the site due to prevailing wind. The industrial origin of $IOA_{metal-7}$ is further supported by the large contribution of Na^+ (60 %), Ni^+ (52 %), and V^+ (∼ 100 %) signals to this factor (Fig. 9). By assuming the same RIE for the metal ions, the V^+/Ni^+ ratio of the $IOA_{metal-7}$ factor is 1.92.

The C_1^+/C_3^+ ratios are similar between $IOA_{metal-7}$ (0.75) and $rBC\text{-}rich_{metal-7}$ (0.73). Although CO_2^+ fragments can be originated from OAs and rBC, CO_2^+ observed in $rBC\text{-}rich_{metal-7}$ and $IOA_{metal-7}$ is likely largely contributed by the refractory soot structure. Both CO_2^+/C_3^+ and $C_3O_2^+/C_3^+$ ratios of $IOA_{metal-7}$ (1.39 and 0.11) are higher than that of $rBC\text{-}rich_{metal-7}$ (0.87 and 0.094), suggesting that more oxygenated refractory soot structures of rBC-containing particles were emitted from industry and shipping emissions. As both $IOA_{metal-7}$ and $rBC\text{-}rich_{metal-7}$ are rBC-dominated factors, the Org/rBC ratios of these two factors were estimated by assuming that all signals from CO^+, CO_2^+, and $C_3O_2^+$ contributed to rBC mass ($IOA_{metal-7} \sim 0.2$ and $rBC\text{-}rich_{metal-7} \sim 0.1$). The results indicate that the rBC-dominated particles from industrial emissions ($IOA_{metal-7}$) had thicker POA coatings than those associated with traffic ($rBC\text{-}rich_{metal-7}$), although the differences were not substantial. The size distribution of m/z 23 (Na^+) signals peaked at ∼ 300 nm during the period, with strong influences from industrial emissions (Supplement and Fig. S11), suggesting that the rBC-containing particles in primary industrial emissions may have different size characteristics compared to those emitted from local traffic, which gave rBC peaks at ∼ 180 nm, as reported in the Supplement.

The IOA factor could be resolved starting from $PMF_{metal-5}$, and the temporal variations and mass spectral characteristics remained roughly the same for the IOA factors identified up to the seven-factor solution. By comparing the time series of the rBC-rich and HOA factors determined by $PMF_{metal-4}$ and $PMF_{metal-7}$, $PMF_{metal-7}$ leads to ∼ 16 % and 27 % of rBC and Org reduction in the mass concentrations of the rBC-rich factor, respectively. Reductions in rBC and Org mass concentrations for $HOA_{metal-7}$ were ∼ 48 % and 19 %, respectively, compared to $HOA_{metal-4}$. The differences of the rBC and Org mass concentrations between the sum of rBC-rich and HOA factors (i.e., $rBC\text{-}rich_{metal-7} + HOA_{metal-7}$ vs. $rBC\text{-}rich_{metal-4} + HOA_{metal-4}$ with $R_{ts} = 0.97$ and 0.98 for rBC and OA masses, respectively) were ∼ 20 % and 22 %, respectively. Although it is not straightforward to interpret the splitting of factors from $PMF_{metal-4}$ to $PMF_{metal-7}$, most of the $IOA_{metal-7}$ mass was likely extracted from the rBC-rich and HOA factors. This speculation is supported by our observation that the rBC and Org mass concentrations of these primary factors from $PMF_{metal-4}$ and $PMF_{metal-7}$ are strongly correlated (i.e., $rBC\text{-}rich_{metal-7} + HOA_{metal-7} + IOA_{metal-7}$ vs. $rBC\text{-}rich_{metal-4} + HOA_{metal-4}$ with $R_{ts} > 0.99$) and are comparable between the two PMF scenarios, with only ∼ 1.5 % and 6.9 % differences for rBC and Org mass, respectively.

Our analysis demonstrates that Na^+, Ni^+, and V^+ play a key role in driving the separation of industrial-related combustion emissions for rBC-containing particles from traffic emissions in urban environments that cannot be achieved by PMF_{base} due to non-distinctive rBC and/or OA mass spectral characteristics between local combustion sources. The total rBC mass was largely assigned to $rBC\text{-}rich_{metal-7}$ (71 %), followed by $IOA_{metal-7}$ (10 %) and $HOA_{metal-7}$ (4 %), and these primary factors accounted for ∼ 44 % of the total OA mass ($HOA_{metal-7}$: 26 %, $rBC\text{-}rich_{metal-7}$: 13 %, and $IOA_{metal-7}$: 5 %) on average for the whole period of study, as shown in Fig. 8. Using the mean values of their diurnal patterns, it can be estimated that $IOA_{metal-7}$ contributed up to ∼ 20 % of the total rBC and OA mass emitted from the three anthropogenic primary combustion sources during the

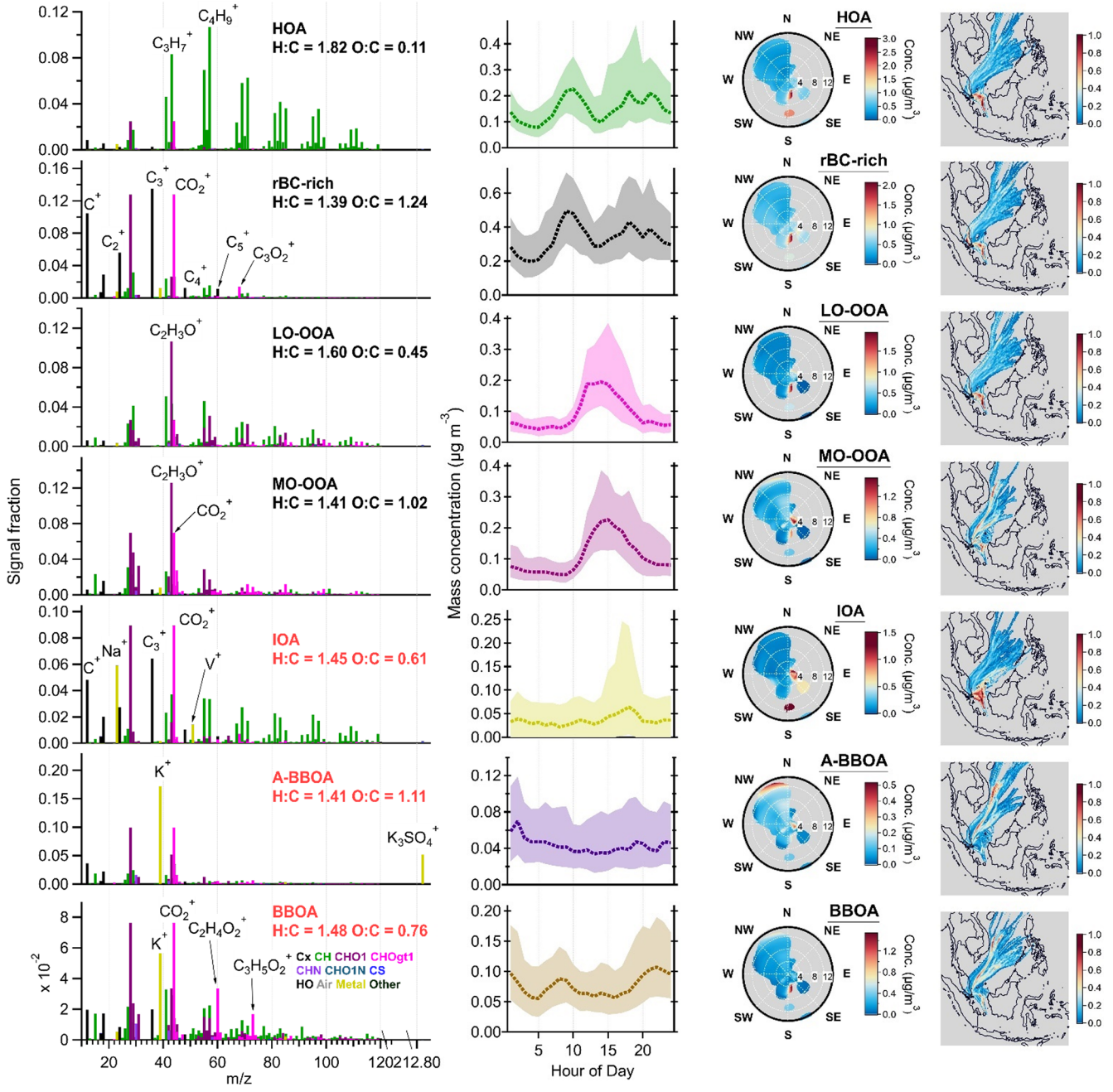

Figure 10. Results of $PMF_{metal-7}$ factors: mass spectra of OAs, rBC and metal (first column), diurnal cycles of mass concentrations (second column, median: dashed lines, 25th/75th percentiles: shaded areas), NWR plots (third column), and PSCF plots (fourth column). The PMF mass spectra were not RIE-adjusted for different species. K^+ signal intensities were downscaled by a factor of 10 for visualization purposes. The wind speed unit in the NWR plots (radial axis) is $m\,s^{-1}$. The color scale of the NWR plots represents the species concentration ($\mu g\,m^{-3}$). Some of the NWR plots are presented with different wind speed ranges ($< 3\,m\,s^{-1}$) and resolutions in Fig. S10.

period with strong industrial influences in the afternoon (i.e., ~ 80 % from $rBC\text{-}rich_{metal-7}$ and $HOA_{metal-7}$), whereas the background contribution of $IOA_{metal-7}$ varied between 8 % and 13 %. It is worth noting that industrial influences might not be completely separated from the $rBC\text{-}rich_{metal-7}$ and $HOA_{metal-7}$ factors in this study due to the similar mass spectral characteristics of rBC and OAs emitted from fossil fuel combustion. Therefore, the mass contribution of $IOA_{metal-7}$ probably represents the lower limit at our measurement site. Excluding the period with high IOA mass loadings (i.e., top 25 %) in our PMF_{metal}, IOAs could not be identified, and the rBC-rich and HOA mass loadings in the six-factor solution

were reduced by 15 % and 25 % at 17:00–18:00 LT, respectively.

3.4.2 Identification of rBC-containing particles from transported BB emissions

$PMF_{metal-7}$ identified two biomass-burning-related factors (BBOA and A-BBOA). $BBOA_{metal-7}$ represents the relatively fresh biomass burning emission, as it has a strong signal contribution from the two signature fragments (i.e., $f_{C_2H_4O_2^+} = 3.8\,\%$ and $f_{C_3H_5O_2^+} = 1.9\,\%$). The $BBOA_{metal-7}$ factor is the second-largest contributor of K^+ (25 %) and Rb^+ (38 %) signals (Fig. 9). On the contrary, A-$BBOA_{metal-7}$ likely represents the relatively aged BBOA. A-$BBOA_{metal-7}$ contributed to over 60 % of K^+ and Rb^+ and accounted for 93 % of $K_3SO_4^+$. As discussed in Sect. 3.2.1, $K_3SO_4^+$ has been used as a signature ion for aged biomass burning emissions due to the heterogeneous conversion of potassium salt to K_2SO_4. During atmospheric aging, OAs in biomass burning emissions can be oxidized to diminish the signature fragments (i.e., $C_2H_4O_2^+$) and to produce highly oxygenated OAs that can be indicated by the CO_2^+ organic fragments (Cubison et al., 2011). This phenomenon is well-aligned with our observation that A-$BBOA_{metal-7}$ consists of more highly oxidized OA (i.e., O : C = 1.11 and strong signals at CO_2^+) and a lower value of $f_{C_2H_4O_2^+}$ (0.9 %) compared to those of $BBOA_{metal-7}$. As illustrated in Fig. 11, the $f_{C_2H_4O_2^+}$ values for $BBOA_{metal-7}$ and A-$BBOA_{metal-7}$ became 1.5 % and 0.3 %, respectively, with the conversion factor applied (Ma et al., 2021). The data without applying the conversion factor are shown in Fig. S12. The hotspots of $BBOA_{metal-7}$ and A-$BBOA_{metal-7}$ in the PSCF plots suggest the regional transport of these two types of rBC-containing particles from northeast of Singapore (Fig. 10).

The contribution of LO-OOAs and MO-OOAs derived from $PMF_{metal-7}$ to the total OA mass reduced by 5 % and 7 %, respectively, compared to the case of $PMF_{based-4}$ (Fig. 8). As discussed in Sect. 3.3.2, $MO\text{-}OOA_{base-4}$ represents the more oxidized SOA that was influenced by both local photochemistry and regional transport of biomass burning emissions, whereas $LO\text{-}OOA_{base-4}$ is primarily associated with local photochemical production. By comparing the results between $PMF_{metal-4}$ and $PMF_{metal-7}$, $PMF_{metal-7}$ leads to a reduction of ∼ 58 % and 23 % of rBC and OA mass concentrations, respectively, for the sum of these two OOA factors (i.e., $LO\text{-}OOA_{metal-7} + MO\text{-}OOA_{metal-7}$ vs. $LO\text{-}OOA_{metal-4} + MO\text{-}OOA_{metal-4}$, with $R_{ts} = 0.93$ and 0.97 for rBC and OA masses, respectively), which were mainly redistributed to the $BBOA_{metal-7}$ and A-$BBOA_{metal-7}$ factors. There were only within less than 2 % differences on average between the total rBC and OA mass concentrations of these factors derived from $PMF_{metal-4}$ and $PMF_{metal-7}$ (i.e., $LO\text{-}OOA_{metal-7} + MO\text{-}OOA_{metal-7} + BBOA_{metal-7} + A\text{-}BBOA_{metal-7}$ vs. $LO\text{-}OOA_{metal-4} + MO\text{-}OOA_{metal-4}$, with $R_{ts} = 0.98$ and > 0.99 for rBC and OA masses, respectively). The above results show that PMF_{metal} can allow better separation of aged/more oxidized biomass-burning-related rBC-containing particles from locally formed and background SOA materials at our measurement site. This is further supported by our observation that the $f_{C_2H_4O_2^+}$ values of $MO\text{-}OOA_{metal-7}$ substantially dropped to 0.1 % compared to that of $MO\text{-}OOA_{base-4}$ (0.5 %, Fig. 11).

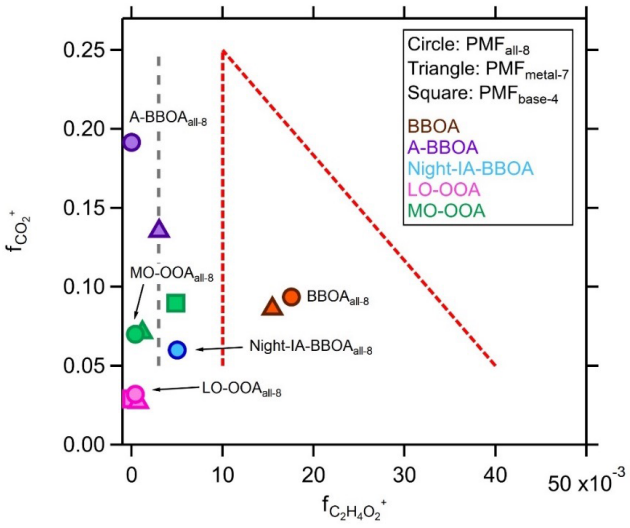

Figure 11. The $f_{CO_2^+}$ vs. $f_{C_2H_4O_2^+}$ plot for evaluating OOA and biomass-burning-related OA factors derived from different PMF scenarios. The conversion factor of 2.45 derived by Ma et al. (2021) was applied to the $f_{C_2H_4O_2^+}$ values for more direct comparison with the observational-based framework derived by Cubison et al. (2011). The data without conversion are reported in Fig. S12. The gray dashed line represents the background level (0.3 %) of $f_{C_2H_4O_2^+}$ for OAs without a significant biomass burning signature reported by Cubison et al. (2011). Red dashed lines represent the boundaries of the triangular region that cover the BBOAs observed by Cubison et al. (2011).

3.5 Additional insight into SOA chemistry and aging of POA based on PMF_{all}

Previous studies have shown that including IA species related to secondary processes in the PMF analysis of standard HR-AMS measurements can provide further insights into source separation and characteristics (Day et al., 2022; Ng et al., 2017; Sun et al., 2012; Xu et al., 2015). This section focuses on integrating a few IA components, including fragments from SO_4^{2-}, NO_3^-, and Cl^-, into the PMF_{metal} to explore whether the understanding of the secondary aerosol coating formation and aging chemistry of rBC-containing particles can be improved. Similar to PMF_{base-4}, PMF_{all-4} yields the rBC-rich, HOA, LO-OOA, and MO-OOA factors, and all of them correlate well with the corresponding PMF_{base-4} factors ($R_{m/z} > 0.98$ and $R_{ts} > 0.98$, Table S4), suggesting high

consistency between all the four-factor PMF scenarios (i.e., PMF_{base-4}, $PMF_{metal-4}$, and PMF_{all-4}). The physical meaning of higher number factors for PMF_{all} was explored, and PMF_{all-8} was considered as the optimum solution. These four basic factors identified by PMF_{all-4} also gave similar time series compared to those corresponding factors determined by PMF_{all-8} ($R_{ts} > 0.94$, Table S6).

PMF_{all-8} was also able to identify the same seven factors as $PMF_{metal-7}$ and to further separate a biomass-burning-influenced OA factor that was associated with different IA fragments (denoted as Night-IA-$BBOA_{all-8}$ hereafter). Integrating IA fragments into the PMF analysis did not make a significant impact on the distribution of metal ions in fossil and biomass combustion emissions (Fig. 12). IOA_{all-8} is still the largest contributor to Na^+, V^+, and Ni^+. $BBOA_{all-8}$ and A-$BBOA_{all-8}$ remain the two main contributors to K^+, Rb^+, and $K_3SO_4^+$ (Figs. 9 and 12). According to the CO_2^+/C_3^+ and $C_3O_2^+/C_3^+$ ratios, the IOA_{all-8} factor (1.23 and 0.10) contained more oxygenated refractory soot structures compared to that associated with the rBC-$rich_{all-8}$ factor (0.82 and 0.09), which is also similar to the results of $PMF_{metal-7}$ (Sect. 3.4.1). As reported in Table S3, the Org/BC ratios of rBC-rich, IOA, and LO-OOA between $PMF_{metal-7}$ and PMF_{all-8} remain roughly the same, whereas the ratios of HOA, MO-OOA, and BBOA decreased or increased by 23 %–32 %. The Org/rBC ratio of A-$BBOA_{all-8}$ is about 2.5 times higher than that of A-$BBOA_{metal-7}$. Overall, most of the rBC mass (∼ 78 %, i.e., rBC-$rich_{all-8}$ + IOA_{all-8}) was thinly coated by OAs (i.e., Org/rBC < 1), and only ∼ 4 % of the rBC mass was thickly coated by HOA_{all-8} and LO-OOA_{all-8} materials (Org/rBC > 13.9). rBC mass associated with MO-OOA_{all-8}, and all the BBOA-related factors identified by PMF_{all-8} (∼ 18 %) were moderately coated by OAs (Org/rBC = 2.3–7.4, see Supplement for coating thickness estimation and Table S2).

3.5.1 Identification of BBOAs associated with IA chemistry

Night-IA-$BBOA_{all-8}$ accounted for 7 % and 9 % of the total rBC and OA mass, respectively (Fig. 8). Figure 12 shows that 6 %, 13 %, 12 %, and 9 % of Na^+, K^+, Ni^+, and Rb^+, respectively, are allocated to the Night-IA-$BBOA_{all-8}$ factor, suggesting that this factor could have experienced mixed influences from both industrial and biomass burning sources. Furthermore, the major IA fragments in $BBOA_{all-7}$ (48 %, 39 %, and 63 % of SO_4^{2-}, NO_3^-, and Cl^-, respectively) were largely redistributed to Night-IA-$BBOA_{all-8}$ (43 %, 40 %, and 60 % of SO_4^{2-}, NO_3^-, and Cl^-, respectively). Together with the diurnal pattern of Night-IA-$BBOA_{all-8}$ (Fig. 13), our observation suggests that Night-IA-$BBOA_{all-8}$ was more associated with the formation and/or condensation of secondary IAs at night before they reached the sampling site. A-$BBOA_{all-8}$ is another factor that had observable contributions to the three major inorganic components (4 %, 29 %, and 20 % of SO_4^{2-}, NO_3^-, and Cl^-, respectively).

The mixed influences from multiple emissions and aging processes were also reflected by the relatively even reduction in OA masses of the rBC-rich, MO-OOA, and BBOA-related factors (∼ 3 % each) compared to the results of $PMF_{metal-7}$ (Fig. 8). Comparing to MO-$OOA_{metal-7}$, separation of Night-IA-$BBOA_{all-8}$ from other OOA components led to a ∼ 28 % reduction in MO-OOA_{all-8} background mass concentrations between midnight and early morning (i.e., from ∼ 0.06 to 0.04 µg m^{-3}). In contrast, no obvious changes in background levels of LO-OOAs were observed between the $PMF_{metal-7}$ and PMF_{all-8} solutions (i.e., 0.05 µg m^{-3} for both cases). In addition to the contribution of Na^+ and Ni^+, a clear mass spectral pattern of hydrocarbon peaks (i.e., C_xH_y) was observed for Night-IA-$BBOA_{all-8}$ and was similar to that observed in HOA_{all-8} and rBC-$rich_{all-8}$. The relatively high H : C ratio (1.66) and low OS_c (−0.26) of Night-IA-$BBOA_{all-8}$ compared to other PMF_{all-8} factors also indicate the contribution of POAs from combustion emissions to this nighttime factor. These observations illustrate the possible involvement of fossil-fuel-combustion-related POAs in nighttime chemistry, although their emissions were relatively low at midnight in general. The $f_{C_2H_4O_2^+}$ value of Night-IA-$BBOA_{all-8}$ is 0.5 % (or 1.3 % without the conversion factor applied). This BBOA signature fragment is still slightly higher than the background levels for typical POAs and SOAs (Cubison et al., 2011), although they might have experienced extensive mixing with other aerosol components and/or atmospheric processing at nighttime (Figs. 11 and S11).

$BBOA_{all-8}$ retained the signature organic fragments of biomass burning emissions ($f_{C_2H_4O_2^+}$ = 1.8 % or 4.3 % without the conversion factor applied), whereas almost no $f_{C_2H_4O_2^+}$ was observed in A-$BBOA_{all-8}$, likely due to the improved separation of more aged BBOA components from the fresher biomass burning emissions in the PMF_{all-8} solution. Nevertheless, A-$BBOA_{all-8}$ remained the most important contributor to K^+, Rb^+, and $K_3SO_4^+$, which continues to support our hypothesis that A-BBOAs likely represent the heavily aged OAs in biomass burning emissions. These observations further highlight the importance of including metal-related ions for PMF analysis of OA coated on an rBC core for source apportionment analysis. The origin of heavily aged/oxidized biomass-burning-related OA materials (e.g., A-BBOAs identified in this work) cannot be easily identified based on the observational-based framework (f_{44} vs. f_{60} or $f_{CO_2^+}$ vs. $f_{C_2H_4O_2^+}$) developed by Cubison et al. (2011) alone, as the signature BBOA fragments can be completely diminished after extensive aging. Such additional information is required to better understand the atmospheric fate and transformation of OAs in biomass burning emissions and how they may affect their contribution to the highly oxidized back-

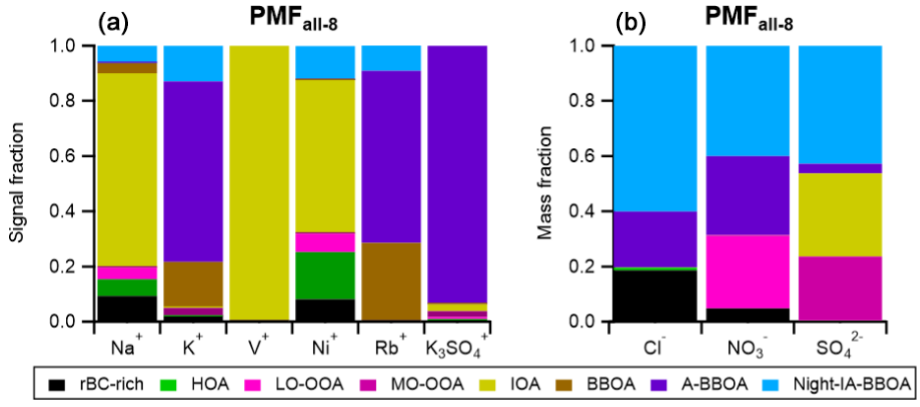

Figure 12. Metal **(a)** and IA component **(b)** contributions to individual factors identified by PMF_{all-8}.

ground SOA materials in various locations, as demonstrated in this work.

3.5.2 Insight from nitrate and sulfate fragments

Figure 12 shows that NO_3^- mass was mainly assigned to Night-IA-$BBOA_{all-8}$ (40 %), A-$BBOA_{all-8}$ (29 %), and LO-OOA_{all-8} (26 %). As discussed in Sect. 3.2.3, the NO^+/NO_2^+ ratio can be used as an indicator to evaluate the relative importance of organo-nitrate and inorganic nitrate. The NO^+/NO_2^+ ratios for LO-OOA_{all-8}, A-$BBOA_{all-8}$, and Night-IA-$BBOA_{all-8}$ were 0.8, 1.7, and 3.3, respectively. Although the separation of organo-nitrate and inorganic nitrate in $NR\text{-}PM_{coating}$ determined by the LV scheme of SP-AMS remains non-quantitative due to the different fragmentation for compounds vaporized by TV and LV (Ma et al., 2021), there are two major implications for these observations. Firstly, the NO^+/NO_2^+ ratio of LO-OOA_{all-8} was close to the one for NH_4NO_3 coated on rBC cores (0.9) determined during our SP-AMS calibration. As LO-OOA_{all-8} mainly represents the freshly formed SOAs due to local photooxidation, our results suggest that inorganic nitrate and fresh SOAs with a lower degree of oxygenation (i.e., LO-OOA_{all-8}) were likely produced together via photooxidation of NO_2 and gaseous SOA precursors, and they subsequently condensed on the rBC particles in a local timescale. Secondly, the relatively high NO^+/NO_2^+ ratio of the A-$BBOA_{all-8}$ and Night-IA-$BBOA_{all-8}$ factors indicates that organo-nitrate compounds can be significant contributors to the observed NO^+ and NO_2^+ signals in these factors. This is well-aligned with recent laboratory studies showing that nocturnal NO_3 radical chemistry of different SOA precursors, including those emitted from biomass burning, can be a secondary source of organo-nitrate compounds (Fry et al., 2018; Kodros et al., 2020; Yazdani et al., 2023).

The majority of SO_4^{2-} mass was assigned to Night-IA-$BBOA_{all-8}$ (42 %), IOA_{all-8} (30 %), and MO-OOA_{all-8} (23 %), as shown in Fig. 12. There are two implications from this observation that may require further investigation. Firstly, although IOA_{all-8} is expected to be primary in nature, the relatively large contribution of this factor to SO_4^{2-} mass suggests that the rBC-containing particles from industry may act as a condensation sink of acidic sulfate that is locally formed through photooxidation of gaseous SO_2 in the pollutant plumes emitted from industry. Our results show that LO-OOAs and MO-OOAs represent freshly formed SOAs due to the strong solar radiation in the afternoon in all PMF cases. PMF_{all-8} further suggests that the formation of LO-OOA_{all-8} and MO-OOA_{all-8} was likely concurrent with nitrate and sulfate formation chemistry, respectively, in daytime. The formation of these two types of OOA particles might be due to the mixing of different gaseous precursors in the pollutant plumes near sources and during atmospheric transport. Secondly, in general, our findings show that both A-$BBOA_{all-8}$ and Night-IA-$BBOA_{all-8}$ were the key contributors of the Cl^- and NO_3^- components, whereas there was a large difference in SO_4^{2-} mass contribution between the two factors. Despite the fact that the SO_4^{2-} contribution from A-$BBOA_{all-8}$ was relatively small, A-$BBOA_{all-8}$ accounted for 93 % of $K_3SO_4^+$ signals, indicating the association of SO_4^{2-} formation chemistry with this factor. As K_2SO_4 can be formed via reactions of acidic sulfate with other potassium salts (e.g., KCl) in biomass burning emissions, these observations imply that different forms of sulfate fragments measured by the SP-AMS may be able to evaluate the atmospheric aging of biomass burning emissions involving interaction with acidic sulfate. Overall, our observations highlight the importance of studying the interaction of the SOA and IA formation chemistry and aerosol mixing state in such complex urban environments.

3.6 PMF comparison between ACSM and SP-AMS measurement

PMF analysis of OAs measured by ACSM was performed. Up to a 10-factor solution was evaluated, and a four-factor solution was selected (referred as PMF_{ACSM}; see Supple-

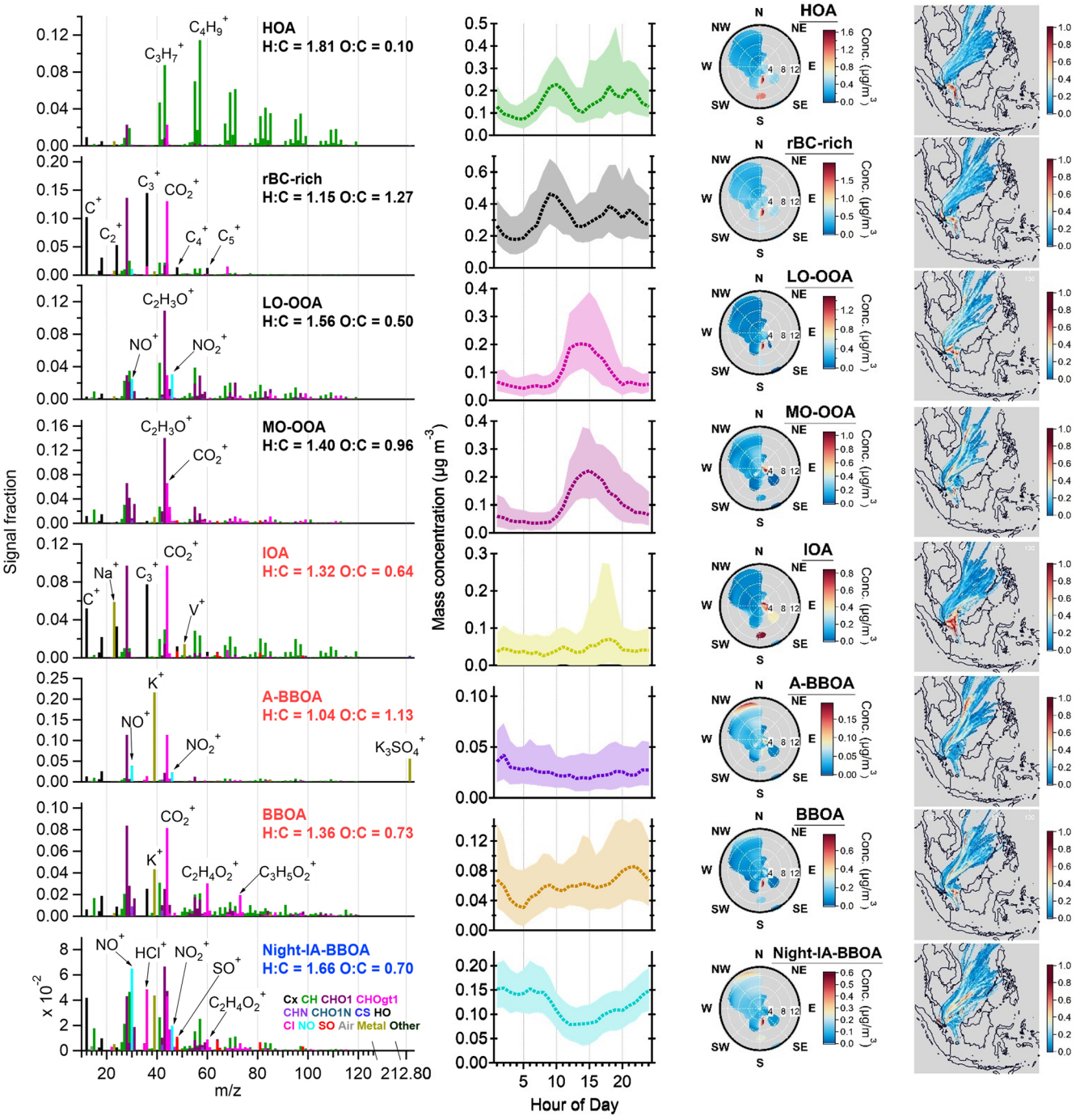

Figure 13. Results of PMF_{all-8} factors: mass spectra of OA, rBC, metal, and IA (first column), diurnal cycles of mass concentrations (second column, median: dashed lines, 25th/75th percentiles: shaded areas), NWR plots (third column), and PSCF plots (fourth column). The PMF mass spectra were not RIE-adjusted for different species. K^+ signal intensities were downscaled by a factor of 10 for visualization purposes. The wind speed unit in the NWR plots (radial axis) is $m\,s^{-1}$. The color scale of the NWR plots represents the species concentration ($\mu g\,m^{-3}$). Some of the NWR plots are presented in different wind speed ranges ($< 3\,m\,s^{-1}$) and resolutions in Fig. S13.

ment for details). The four factors include HOAs, cooking-related OAs (COAs), BBOAs, and OOAs. The subscript "ACSM" indicates the PMF factors (i.e., HOA_{ACSM}) identified by ACSM measurements in the subsequent discussion. The mass spectral profiles, diurnal patterns, NWR plots, and PSCF plots of these four factors are reported in Fig. S14. The PMF_{ACSM} and PMF_{all-8} results are compared to improve our understanding of the fractional contribution of OA coating to the major OA factors identified by the ACSM measurement. Given that PMF_{all-8} identifies more factors than PMF_{ACSM}, some of the PMF_{all-8} factors are combined based on their sources and emissions characteristics for the comparison.

According to the mass spectral profile and diurnal pattern of HOA_{ACSM}, this factor mainly represents POAs emitted from multiple local combustion sources, including traffic and industrial emissions. Unlike PMF_{all-8}, where rBC and metal fragments can improve the separation of HOA_{base-4} into various local combustion emissions (i.e., $HOA_{coating} \approx HOA_{all-8} + rBC\text{-}rich_{all-8} + IOA_{all-8}$), HOA_{ACSM} could not be further resolved by PMF_{ACSM} due to the lack of a distinctive OA fragment fingerprint between fossil combustion sources. Comparison of the time series of OA mass concentrations between HOA_{ACSM} and $HOA_{coating}$ ($R = 0.85$, slope $= 0.69$) suggests that approximately 69 % of HOA_{ACSM} was coated on the rBC surface. Previous studies have reported similar fractional contributions of $HOA_{coating}$ to the total HOAs in NR-PM_1, ranging from 64 % to ∼ 100 %, in other urban and near-road environments (Cui et al., 2022; Lee et al., 2017; Massoli et al., 2012, 2015; Wang et al., 2020). Figure S14 shows that cooking OAs (COA_{ACSM}) peaked at lunch and dinner time. COA is a POA component commonly observed in urban environments and was also identified in our previous study at the same location using an SP-AMS operated by a DV mode SP-AMS (Rivellini et al., 2020). Given that COAs were not identified in NR-$PM_{coating}$, our observation suggests that COA_{ACSM} was negligibly internally mixed with rBC, consistent with findings from other urban environments (Cui et al., 2022; Farley et al., 2024; Lee et al., 2017; Willis et al., 2016).

OOA_{ACSM} represents both fresh SOAs produced through local photochemistry and aged SOAs from the background. The sum of OA mass concentrations of LO-OOA_{all-8}, MO-OOA_{all-8}, and A-$BBOA_{all-8}$ (i.e., $OOA_{coating} \approx$ LO-OOA_{all-8} + MO-OO_{all-8} + A-$BBOA_{all-8}$) was considered as the major SOA coating component due to their diurnal features caused by photochemistry (i.e., peak between 13:00 and 15:00 LT) and/or their highly oxygenated OA compositions. A-$BBOA_{all-8}$ was included as a portion of $OOA_{coating}$, as this factor is dominated by CO^+ and CO_2^+ OA fragments and exhibits the highest O : C ratio among the PMF_{all-8} factors, indicating significant atmospheric aging. $OOA_{coating}$ had a strong correlation against OOA_{ACSM} ($R = 0.86$, slope $= 0.21$), indicating that rBC particles were a condensation sink of ∼ 21 % of SOAs in this study. Previous studies have reported a similar fractional contribution of $OOA_{coating}$ (20 %–60 %) to the total OOAs in NR-PM_1 at other locations (Cui et al., 2022; Lee et al., 2017; Wang et al., 2020).

Lastly, $BBOA_{ACSM}$, an OA component characterized by relatively strong signals at m/z 60, was compared to the sum of OA mass in $BBOA_{all-8}$ and Night-IA-$BBOA_{all-8}$ (i.e., $BBOA_{coating} \approx BBOA_{all-8}$ + Night-IA-$BBOA_{all-8}$). Despite rBC and OAs being largely co-emitted from biomass burning, a moderate correlation between $BBOA_{ACSM}$ and $BBOA_{coating}$ was observed ($R = 0.63$, slope $= 0.27$), and only ∼ 27 % of $BBOA_{ACSM}$ was coated on rBC particles. The fractional contribution of $BBOA_{coating}$ to $BBOA_{ACSM}$ increased by 2 % only if A-$BBOA_{all-8}$ was included in the $BBOA_{coating}$ mass concentrations. Notably, a few previous SP-AMS studies have reported BBOAs in rBC coating but not in NR-PM_1, highlighting the challenge of identifying BBOA characteristics in both NR-$PM_{coating}$ and NR-PM_1 (Cui et al., 2022; Wang et al., 2020, 2017), as they might experience different degrees of aging and exhibit varying emission characteristics depending on the burning source.

4 Conclusion and atmospheric implications

With an increasing number of SP-AMS measurements reported around the world (Zhang et al., 2020), source apportionment of rBC-containing particles and their associated coating materials based on PMF analysis can improve the understanding of characteristics and atmospheric processing of various combustion emissions and, subsequently, the prediction of their climatic and health impacts. This work demonstrates that including rBC, OA, IA, and metal fragments improves source apportionment and coating thickness quantification (i.e., Org/rBC ratio) of rBC-containing particles in urban environments under strong influences of multiple anthropogenic emissions and provides insight into our understanding of the secondary processing of rBC-containing particles in Singapore, a complex tropical urban environment with large-scale shipping ports and petrochemical industries.

All the PMF scenarios analyzed in this work can identify two primary traffic-related factors (HOAs and rBC-rich OAs), which have been previously reported in other urban and near-road environments across different continents (Cui et al., 2022; Farley et al., 2023; Lee et al., 2017; Saarikoski et al., 2019; Wang et al., 2020). As demonstrated in this work, these two factors may serve as useful indicators for distinguishing rBC emissions from gasoline and diesel vehicles in typical urban settings. This can provide quantitative insights to support the development of targeted air pollution control strategies related to traffic emissions in typical urban environments. Furthermore, the observed variability in the mixing degree between the rBC core and the HOA coating can result in substantial differences in aerosol optical properties and radiative effects compared to the commonly as-

sumed uniform mixing (Willis et al., 2016). The majority of rBC mass classified into the rBC-rich OA factor could be one of the reasons to explain insignificant lensing effects of the BC coating in ambient measurements, but models overestimated the light absorption enhancement of BC coated with OAs in an urban environment even with high bulk R_{BC} values (Cappa et al., 2012; Fierce et al., 2020; Healy et al., 2015; Liu et al., 2017).

This work provides further separation of an industrial-related factor from primary traffic emissions. Although such industrial and shipping emissions are transported to our sampling site occasionally during afternoon sea breeze, the IOA factor accounted for 10 %–12 % of rBC and 5 % of OA coating, suggesting that the negative impacts of industrial emissions on the local air quality should not be overlooked. More importantly, the IOA factor was strongly associated with V^+ and Ni^+, suggesting that this type of rBC-containing particle might pose high potential risks to human health and the environment. This observation is strongly relevant to other coastal cities with major shipping ports and industrial areas with large-scale petrochemical facilities. Recently, Tehrani et al. (2023) conducted mobile SP-AMS measurement in the Chester–Trainer–Marcus Hook area of southeastern Pennsylvania, which is home to multiple petrochemical plants, a refinery, and a waste incinerator, showing elevated heavy metal concentrations (e.g., Sb, As, Cd, and V) near the industrial facilities. It is important to note that anthropogenic OA factors related to industrial, shipping, and coal-combustion emissions have been identified in previous standard AMS studies across various locations (e.g., Chen et al., 2022; Daellenbach et al., 2024; Xu et al., 2014). A deeper understanding of the heavy metal constituents in these emissions could offer valuable insights into their toxicity and broader environmental and public health implications.

Biomass burning emissions have been impacting the air quality and regional haze formation in Southeast Asia (Adam et al., 2021; Budisulistiorini et al., 2018; Othman et al., 2022; Van et al., 2022). This work provides additional insight into understanding the fate and transformation of rBC-containing particles in aged biomass burning emissions. Overall, A-BBOA and Night-IA-BBOA derived from PMF_{all} accounted for 12 % of OA coating mass in total, and the mass contribution of MO-OOAs to total OA coatings decreased from 31 % for PMF_{base} to 24 % and 21 % for PMF_{metal} and PMF_{all}, respectively. It is important to note that MO-OOAs have been consistently reported as a dominant background OA component in total NR-PM_1 across many previous AMS studies (Chen et al., 2022; Jimenez et al., 2009; Zhang et al., 2011, 2020). However, quantifying its contribution from aged POAs, including BBOAs, remains a challenge. Recently, Vasilakopoulou et al. (2023) showed rapid transformation of BBOAs into highly oxidized and harmful background MO-OOAs in Europe. Although this study focused on OA coating characterization, our findings highlight the potential to distinguish highly oxidized BBOA-derived materials from the typical background MO-OOAs in NR-PM_1 identified by standard AMS techniques. This distinction offers a valuable approach for better evaluating the overall health and environmental impacts of aged or transported BBOAs, particularly in Southeast Asia and other regions heavily affected by wildfires and agricultural burning.

Most of the IA species observed in this work were externally mixed rBC particles (i.e., > 95 % IAs were externally mixed). However, including the IA coating materials in the PMF analysis still can provide additional information to advance our understanding of SOA coating formation. PMF_{all} shows concurrent LO-OOA and inorganic nitrate formation via daytime chemistry, suggesting that the LO-OOA formation observed in this work is likely more relevant to the photochemical SOA formation chemistry in the presence of NO_x. On the other hand, the observed linkage between the local photochemical production of MO-OOAs and acidic sulfate particle formation suggests the possibility of co-oxidation of SO_2 and SOA precursors in the industrial-influenced atmosphere. These observations highlight the importance of investigating the interaction of SOA and IA formation chemistry and integrating such details in air quality models and illustrates the need of evaluating the degree of aerosol mixing of rBC and chemical species in NR-$PM_{coating}$ as well as its relationship with different atmospheric processes by utilizing the single particle measurement capability of SP-AMS (Farley et al., 2024; Lee et al., 2019, 2016; Willis et al., 2016).

Data availability. The dataset for this publication is available upon request from the corresponding authors.

Supplement. The supplement related to this article is available online at https://doi.org/10.5194/acp-25-8185-2025-supplement.

Author contributions. AKYL supervised the projects and conceptualized the research goals. MM, LHR, and AKYL planned the field campaign and performed the data analysis. MM and LHR carried out the SP-AMS measurements. YZ, MK, and LEY provided supporting measurement data. MM and AKYL prepared the paper with input from all the co-authors.

Competing interests. At least one of the (co-)authors is a member of the editorial board of *Atmospheric Chemistry and Physics*. The peer-review process was guided by an independent editor, and the authors also have no other competing interests to declare.

Disclaimer. The contents of this paper do not represent the views of the National Environmental Agency of Singapore.

Publisher's note: Copernicus Publications remains neutral

with regard to jurisdictional claims made in the text, published maps, institutional affiliations, or any other geographical representation in this paper. While Copernicus Publications makes every effort to include appropriate place names, the final responsibility lies with the authors.

Acknowledgements. We acknowledge Mikinori Kuwata for providing the ToF-ACSM instrument. We also thank James Allan and the anonymous reviewers for their valuable suggestions and comments, which have helped improve the quality of this paper.

Financial support. This work was supported by the National Environmental Agency of Singapore (NEA; grant no. R-706-000-043-490), the Environment and Climate Change Canada air quality program, and the Cambridge Centre for Carbon Reduction in Chemical Technologies program.

Review statement. This paper was edited by James Allan and reviewed by two anonymous referees.

References

Adam, M. G., Tran, P. T. M., Bolan, N., and Balasubramanian, R.: Biomass burning-derived airborne particulate matter in Southeast Asia: A critical review, J. Hazard. Mater., 407, 124760, https://doi.org/10.1016/j.jhazmat.2020.124760, 2021.

Allan, J. D., Delia, A. E., Coe, H., Bower, K. N., Alfarra, M. R., Jimenez, J. L., Middlebrook, A. M., Drewnick, F., Onasch, T. B., Canagaratna, M. R., Jayne, J. T., and Worsnop, D. R.: A generalised method for the extraction of chemically resolved mass spectra from Aerodyne aerosol mass spectrometer data, J. Aerosol Sci., 35, 909–922, https://doi.org/10.1016/j.jaerosci.2004.02.007, 2004.

Baker, J.: A cluster analysis of long range air transport pathways and associated pollutant concentrations within the UK, Atmos. Environ., 44, 563–571, https://doi.org/10.1016/j.atmosenv.2009.10.030, 2010.

Betha, R., Pradani, M., Lestari, P., Joshi, U. M., Reid, J. S., and Balasubramanian, R.: Chemical speciation of trace metals emitted from Indonesian peat fires for health risk assessment, Atmos. Res., 122, 571–578, https://doi.org/10.1016/j.atmosres.2012.05.024, 2013.

Bibi, Z., Coe, H., Brooks, J., Williams, P. I., Reyes-Villegas, E., Priestley, M., Percival, C. J., and Allan, J. D.: Technical note: A new approach to discriminate different black carbon sources by utilising fullerene and metals in positive matrix factorisation analysis of high-resolution soot particle aerosol mass spectrometer data, Atmos. Chem. Phys., 21, 10763–10777, https://doi.org/10.5194/acp-21-10763-2021, 2021.

Bond, T. C., Doherty, S. J., Fahey, D. W., Forster, P. M., Berntsen, T., DeAngelo, B. J., Flanner, M. G., Ghan, S., Kärcher, B., Koch, D., Kinne, S., Kondo, Y., Quinn, P. K., Sarofim, M. C., Schultz, M. G., Schulz, M., Venkataraman, C., Zhang, H., Zhang, S., Bellouin, N., Guttikunda, S. K., Hopke, P. K., Jacobson, M. Z., Kaiser, J. W., Klimont, Z., Lohmann, U., Schwarz, J. P., Shindell, D., Storelvmo, T., Warren, S. G., and Zender, C. S.: Bounding the role of black carbon in the climate system: A scientific assessment, J. Geophys. Res.-Atmos., 118, 5380–5552, https://doi.org/10.1002/jgrd.50171, 2013.

Borge, R., Lumbreras, J., Vardoulakis, S., Kassomenos, P., and Rodríguez, E.: Analysis of long-range transport influences on urban PM_{10} using two-stage atmospheric trajectory clusters, Atmos. Environ., 41, 4434–4450, https://doi.org/10.1016/j.atmosenv.2007.01.053, 2007.

Budisulistiorini, S. H., Riva, M., Williams, M., Miyakawa, T., Chen, J., Itoh, M., Surratt, J. D., and Kuwata, M.: Dominant contribution of oxygenated organic aerosol to haze particles from real-time observation in Singapore during an Indonesian wildfire event in 2015, Atmos. Chem. Phys., 18, 16481–16498, https://doi.org/10.5194/acp-18-16481-2018, 2018.

Canagaratna, M. R., Jayne, J. T., Jimenez, J. L., Allan, J. D., Alfarra, M. R., Zhang, Q., Onasch, T. B., Drewnick, F., Coe, H., Middlebrook, A., Delia, A., Williams, L. R., Trimborn, A. M., Northway, M. J., DeCarlo, P. F., Kolb, C. E., Davidovits, P., and Worsnop, D. R.: Chemical and microphysical characterization of ambient aerosols with the aerodyne aerosol mass spectrometer, Mass Spectrom. Rev., 26, 185–222, https://doi.org/10.1002/mas.20115, 2007.

Canagaratna, M. R., Jimenez, J. L., Kroll, J. H., Chen, Q., Kessler, S. H., Massoli, P., Hildebrandt Ruiz, L., Fortner, E., Williams, L. R., Wilson, K. R., Surratt, J. D., Donahue, N. M., Jayne, J. T., and Worsnop, D. R.: Elemental ratio measurements of organic compounds using aerosol mass spectrometry: characterization, improved calibration, and implications, Atmos. Chem. Phys., 15, 253–272, https://doi.org/10.5194/acp-15-253-2015, 2015.

Cao, L.-M., Wei, J., He, L.-Y., Zeng, H., Li, M.-L., Zhu, Q., Yu, G.-H., and Huang, X.-F.: Aqueous aging of secondary organic aerosol coating onto black carbon: Insights from simultaneous L-ToF-AMS and SP-AMS measurements at an urban site in southern China, J. Cleaner Prod., 330, 129888, https://doi.org/10.1016/j.jclepro.2021.129888, 2022.

Cappa, C. D., Onasch, T. B., Massoli, P., Worsnop, D. R., Bates, T. S., Cross, E. S., Davidovits, P., Hakala, J., Hayden, K. L., Jobson, B. T., Kolesar, K. R., Lack, D. A., Lerner, B. M., Li, S. M., Mellon, D., Nuaaman, I., Olfert, J. S., Petaja, T., Quinn, P. K., Song, C., Subramanian, R., Williams, E. J., and Zaveri, R. A.: Radiative absorption enhancements due to the mixing state of atmospheric black carbon, Science, 337, 1078–1081, https://doi.org/10.1126/science.1223447, 2012.

Cappa, C. D., Zhang, X., Russell, L. M., Collier, S., Lee, A. K. Y., Chen, C.-L., Betha, R., Chen, S., Liu, J., Price, D. J., Sanchez, K. J., McMeeking, G. R., Williams, L. R., Onasch, T. B., Worsnop, D. R., Abbatt, J., and Zhang, Q.: Light Absorption by Ambient Black and Brown Carbon and its Dependence on Black Carbon Coating State for Two California, USA, Cities in Winter and Summer, J. Geophys. Res.-Atmos., 124, 1550–1577, https://doi.org/10.1029/2018jd029501, 2019.

Carbone, S., Onasch, T., Saarikoski, S., Timonen, H., Saarnio, K., Sueper, D., Rönkkö, T., Pirjola, L., Häyrinen, A., Worsnop, D., and Hillamo, R.: Characterization of trace metals on soot aerosol particles with the SP-AMS: detection and quantification, Atmos. Meas. Tech., 8, 4803–4815, https://doi.org/10.5194/amt-8-4803-2015, 2015.

Carbone, S., Timonen, H. J., Rostedt, A., Happonen, M., Rönkkö, T., Keskinen, J., Ristimaki, J., Korpi, H., Artaxo, P., Canagaratna, M., Worsnop, D., Canonaco, F., Prévôt, A. S. H., Hillamo, R., and Saarikoski, S.: Distinguishing fuel and lubricating oil combustion products in diesel engine exhaust particles, Aerosol Sci. Tech., 53, 594–607, https://doi.org/10.1080/02786826.2019.1584389, 2019.

Chen, G., Canonaco, F., Tobler, A., Aas, W., Alastuey, A., Allan, J., Atabakhsh, S., Aurela, M., Baltensperger, U., Bougiatioti, A., De Brito, J. F., Ceburnis, D., Chazeau, B., Chebaicheb, H., Daellenbach, K. R., Ehn, M., El Haddad, I., Eleftheriadis, K., Favez, O., Flentje, H., Font, A., Fossum, K., Freney, E., Gini, M., Green, D. C., Heikkinen, L., Herrmann, H., Kalogridis, A.-C., Keernik, H., Lhotka, R., Lin, C., Lunder, C., Maasikmets, M., Manousakas, M. I., Marchand, N., Marin, C., Marmureanu, L., Mihalopoulos, N., Moènik, G., Nêcki, J., O'Dowd, C., Ovadnevaite, J., Peter, T., Petit, J.-E., Pikridas, M., Matthew Platt, S., Pokorná, P., Poulain, L., Priestman, M., Riffault, V., Rinaldi, M., Różański, K., Schwarz, J., Sciare, J., Simon, L., Skiba, A., Slowik, J. G., Sosedova, Y., Stavroulas, I., Styszko, K., Teinemaa, E., Timonen, H., Tremper, A., Vasilescu, J., Via, M., Vodièka, P., Wiedensohler, A., Zografou, O., Cruz Minguillón, M., and Prévôt, A. S. H.: European aerosol phenomenology – 8: Harmonised source apportionment of organic aerosol using 22 Year-long ACSM/AMS datasets, Environ. Int., 166, 107325, https://doi.org/10.1016/j.envint.2022.107325, 2022.

China, S., Mazzoleni, C., Gorkowski, K., Aiken, A. C., and Dubey, M. K.: Morphology and mixing state of individual freshly emitted wildfire carbonaceous particles, Nat. Commun., 4, 2122, https://doi.org/10.1038/ncomms3122, 2013.

Collier, S., Williams, L. R., Onasch, T. B., Cappa, C. D., Zhang, X., Russell, L. M., Chen, C.-L., Sanchez, K. J., Worsnop, D. R., and Zhang, Q.: Influence of Emissions and Aqueous Processing on Particles Containing Black Carbon in a Polluted Urban Environment: Insights From a Soot Particle-Aerosol Mass Spectrometer, J. Geophys. Res.-Atmos., 123, 6648–6666, https://doi.org/10.1002/2017jd027851, 2018.

Corbin, J. C., Sierau, B., Gysel, M., Laborde, M., Keller, A., Kim, J., Petzold, A., Onasch, T. B., Lohmann, U., and Mensah, A. A.: Mass spectrometry of refractory black carbon particles from six sources: carbon-cluster and oxygenated ions, Atmos. Chem. Phys., 14, 2591–2603, https://doi.org/10.5194/acp-14-2591-2014, 2014.

Corbin, J. C., Mensah, A. A., Pieber, S. M., Orasche, J., Michalke, B., Zanatta, M., Czech, H., Massabo, D., Buatier de Mongeot, F., Mennucci, C., El Haddad, I., Kumar, N. K., Stengel, B., Huang, Y., Zimmermann, R., Prevot, A. S. H., and Gysel, M.: Trace Metals in Soot and $PM_{2.5}$ from Heavy-Fuel-Oil Combustion in a Marine Engine, Environ. Sci. Technol., 52, 6714–6722, https://doi.org/10.1021/acs.est.8b01764, 2018.

Cubison, M. J., Ortega, A. M., Hayes, P. L., Farmer, D. K., Day, D., Lechner, M. J., Brune, W. H., Apel, E., Diskin, G. S., Fisher, J. A., Fuelberg, H. E., Hecobian, A., Knapp, D. J., Mikoviny, T., Riemer, D., Sachse, G. W., Sessions, W., Weber, R. J., Weinheimer, A. J., Wisthaler, A., and Jimenez, J. L.: Effects of aging on organic aerosol from open biomass burning smoke in aircraft and laboratory studies, Atmos. Chem. Phys., 11, 12049–12064, https://doi.org/10.5194/acp-11-12049-2011, 2011.

Cui, S., Huang, D. D., Wu, Y., Wang, J., Shen, F., Xian, J., Zhang, Y., Wang, H., Huang, C., Liao, H., and Ge, X.: Chemical properties, sources and size-resolved hygroscopicity of submicron black-carbon-containing aerosols in urban Shanghai, Atmos. Chem. Phys., 22, 8073–8096, https://doi.org/10.5194/acp-22-8073-2022, 2022.

Daellenbach, K. R., Cai, J., Hakala, S., Dada, L., Yan, C., Du, W., Yao, L., Zheng, F., Ma, J., Ungeheuer, F., Vogel, A. L., Stolzenburg, D., Hao, Y., Liu, Y., Bianchi, F., Uzu, G., Jaffrezo, J.-L., Worsnop, D. R., Donahue, N. M., and Kulmala, M.: Substantial contribution of transported emissions to organic aerosol in Beijing, Nat. Geosci., 17, 747–754, https://doi.org/10.1038/s41561-024-01493-3, 2024.

Dallmann, T. R., Onasch, T. B., Kirchstetter, T. W., Worton, D. R., Fortner, E. C., Herndon, S. C., Wood, E. C., Franklin, J. P., Worsnop, D. R., Goldstein, A. H., and Harley, R. A.: Characterization of particulate matter emissions from on-road gasoline and diesel vehicles using a soot particle aerosol mass spectrometer, Atmos. Chem. Phys., 14, 7585–7599, https://doi.org/10.5194/acp-14-7585-2014, 2014.

Day, D. A., Campuzano-Jost, P., Nault, B. A., Palm, B. B., Hu, W., Guo, H., Wooldridge, P. J., Cohen, R. C., Docherty, K. S., Huffman, J. A., de Sá, S. S., Martin, S. T., and Jimenez, J. L.: A systematic re-evaluation of methods for quantification of bulk particle-phase organic nitrates using real-time aerosol mass spectrometry, Atmos. Meas. Tech., 15, 459–483, https://doi.org/10.5194/amt-15-459-2022, 2022.

DeCarlo, P. F., Kimmel, J. R., Trimborn, A., Northway, M. J., Jayne, J. T., Aiken, A. C., Gonin, M., Fuhrer, K., Horvath, T., Docherty, K. S., Worsnop, D. R., and Jimenez, J. L.: Field-deployable, high-resolution, time-of-flight aerosol mass spectrometer, Anal. Chem., 78, 8281–8289, https://doi.org/10.1021/ac061249n, 2006.

Draxler, R. R. and Hess, G. D.: . An overview of the HYSPLIT_4 modelling system for trajectories, dispersion and deposition. Aust. Meteor. Mag., 47, 295–308, 1998.

Drinovec, L., Močnik, G., Zotter, P., Prévôt, A. S. H., Ruckstuhl, C., Coz, E., Rupakheti, M., Sciare, J., Müller, T., Wiedensohler, A., and Hansen, A. D. A.: The "dual-spot" Aethalometer: an improved measurement of aerosol black carbon with real-time loading compensation, Atmos. Meas. Tech., 8, 1965–1979, https://doi.org/10.5194/amt-8-1965-2015, 2015.

Farley, R. N., Collier, S., Cappa, C. D., Williams, L. R., Onasch, T. B., Russell, L. M., Kim, H., and Zhang, Q.: Source apportionment of soot particles and aqueous-phase processing of black carbon coatings in an urban environment, Atmos. Chem. Phys., 23, 15039–15056, https://doi.org/10.5194/acp-23-15039-2023, 2023.

Farley, R. N., Lee, J. E., Rivellini, L.-H., Lee, A. K. Y., Dal Porto, R., Cappa, C. D., Gorkowski, K., Shawon, A. S. M., Benedict, K. B., Aiken, A. C., Dubey, M. K., and Zhang, Q.: Chemical properties and single-particle mixing state of soot aerosol in Houston during the TRACER campaign, Atmos. Chem. Phys., 24, 3953–3971, https://doi.org/10.5194/acp-24-3953-2024, 2024.

Farmer, D. K., Matsunaga, A., Docherty, K. S., Surratt, J. D., Seinfeld, J. H., Ziemann, P. J., and Jimenez, J. L.: Response of an aerosol mass spectrometer to organonitrates and organosulfates and implications for atmospheric

chemistry, P Natl. Acad. Sci. USA, 107, 6670–6675, https://doi.org/10.1073/pnas.0912340107, 2010.

Fierce, L., Bond, T. C., Bauer, S. E., Mena, F., and Riemer, N.: Black carbon absorption at the global scale is affected by particle-scale diversity in composition, Nat. Commun., 7, 12361, https://doi.org/10.1038/ncomms12361, 2016.

Fierce, L., Onasch, T. B., Cappa, C. D., Mazzoleni, C., China, S., Bhandari, J., Davidovits, P., Fischer, D. A., Helgestad, T., Lambe, A. T., Sedlacek, A. J., Smith, G. D., and Wolff, L.: Radiative absorption enhancements by black carbon controlled by particle-to-particle heterogeneity in composition, P. Natl. Acad. Sci. USA, 117, 5196–5203, https://doi.org/10.1073/pnas.1919723117, 2020.

Fröhlich, R., Cubison, M. J., Slowik, J. G., Bukowiecki, N., Prévôt, A. S. H., Baltensperger, U., Schneider, J., Kimmel, J. R., Gonin, M., Rohner, U., Worsnop, D. R., and Jayne, J. T.: The ToF-ACSM: a portable aerosol chemical speciation monitor with TOFMS detection, Atmos. Meas. Tech., 6, 3225–3241, https://doi.org/10.5194/amt-6-3225-2013, 2013.

Fry, J. L., Brown, S. S., Middlebrook, A. M., Edwards, P. M., Campuzano-Jost, P., Day, D. A., Jimenez, J. L., Allen, H. M., Ryerson, T. B., Pollack, I., Graus, M., Warneke, C., de Gouw, J. A., Brock, C. A., Gilman, J., Lerner, B. M., Dubé, W. P., Liao, J., and Welti, A.: Secondary organic aerosol (SOA) yields from NO3 radical + isoprene based on nighttime aircraft power plant plume transects, Atmos. Chem. Phys., 18, 11663–11682, https://doi.org/10.5194/acp-18-11663-2018, 2018.

Fwa, T. F., Ang, B. W., and Goh, T. N.: Characteristics of truck traffic in Singapore, J. Adv. Transport., 30, 25–46, https://doi.org/10.1002/atr.5670300204, 1996.

Ge, X., Setyan, A., Sun, Y., and Zhang, Q.: Primary and secondary organic aerosols in Fresno, California during wintertime: Results from high resolution aerosol mass spectrometry, J. Geophys. Res.-Atmos., 117, D19301, https://doi.org/10.1029/2012jd018026, 2012.

Gentner, D. R., Jathar, S. H., Gordon, T. D., Bahreini, R., Day, D. A., El Haddad, I., Hayes, P. L., Pieber, S. M., Platt, S. M., de Gouw, J., Goldstein, A. H., Harley, R. A., Jimenez, J. L., Prevot, A. S., and Robinson, A. L.: Review of Urban Secondary Organic Aerosol Formation from Gasoline and Diesel Motor Vehicle Emissions, Environ. Sci. Technol., 51, 1074–1093, https://doi.org/10.1021/acs.est.6b04509, 2017.

Hansen, A. D. A., Rosen, H., and Novakov, T.: The aethalometer – An instrument for the real-time measurement of optical absorption by aerosol particles, Sci. Total Environ., 36, 191–196, https://doi.org/10.1016/0048-9697(84)90265-1, 1984.

Healy, R. M., Wang, J. M., Jeong, C. H., Lee, A. K. Y., Willis, M. D., Jaroudi, E., Zimmerman, N., Hilker, N., Murphy, M., Eckhardt, S., Stohl, A., Abbatt, J. P. D., Wenger, J. C., and Evans, G. J.: Light-absorbing properties of ambient black carbon and brown carbon from fossil fuel and biomass burning sources, J. Geophys. Res.-Atmos., 120, 6619–6633, https://doi.org/10.1002/2015jd023382, 2015.

Heil, A. and Goldammer, J.: Smoke-haze pollution: a review of the 1997 episode in Southeast Asia, Reg. Environ. Change, 2, 24–37, https://doi.org/10.1007/s101130100021, 2001.

Henry, R., Norris, G. A., Vedantham, R., and Turner, J. R.: Source Region Identification Using Kernel Smoothing, Environ. Sci. Technol., 43, 4090–4097, https://doi.org/10.1021/es8011723, 2009.

Jaafar, S. A., Latif, M. T., Razak, I. S., Wahid, N. B. A., Khan, M. F., and Srithawirat, T.: Composition of carbohydrates, surfactants, major elements and anions in $PM_{2.5}$ during the 2013 Southeast Asia high pollution episode in Malaysia, Particuology, 37, 119–126, https://doi.org/10.1016/j.partic.2017.04.012, 2018.

Jimenez, J. L., Jayne, J. T., Shi, Q., Kolb, C. E., Worsnop, D. R., Yourshaw, I., Seinfeld, J. H., Flagan, R. C., Zhang, X., Smith, K. A., Morris, J. W., and Davidovits, P.: Ambient aerosol sampling using the Aerodyne Aerosol Mass Spectrometer, J. Geophys. Res.-Atmos., 108, 8425, https://doi.org/10.1029/2001JD001213, 2003.

Jimenez, J. L., Canagaratna, M. R., Donahue, N. M., Prevot, A. S., Zhang, Q., Kroll, J. H., DeCarlo, P. F., Allan, J. D., Coe, H., Ng, N. L., Aiken, A. C., Docherty, K. S., Ulbrich, I. M., Grieshop, A. P., Robinson, A. L., Duplissy, J., Smith, J. D., Wilson, K. R., Lanz, V. A., Hueglin, C., Sun, Y. L., Tian, J., Laaksonen, A., Raatikainen, T., Rautiainen, J., Vaattovaara, P., Ehn, M., Kulmala, M., Tomlinson, J. M., Collins, D. R., Cubison, M. J., Dunlea, E. J., Huffman, J. A., Onasch, T. B., Alfarra, M. R., Williams, P. I., Bower, K., Kondo, Y., Schneider, J., Drewnick, F., Borrmann, S., Weimer, S., Demerjian, K., Salcedo, D., Cottrell, L., Griffin, R., Takami, A., Miyoshi, T., Hatakeyama, S., Shimono, A., Sun, J. Y., Zhang, Y. M., Dzepina, K., Kimmel, J. R., Sueper, D., Jayne, J. T., Herndon, S. C., Trimborn, A. M., Williams, L. R., Wood, E. C., Middlebrook, A. M., Kolb, C. E., Baltensperger, U., and Worsnop, D. R.: Evolution of organic aerosols in the atmosphere, Science, 326, 1525–1529, https://doi.org/10.1126/science.1180353, 2009.

Kodros, J. K., Papanastasiou, D. K., Paglione, M., Masiol, M., Squizzato, S., Florou, K., Skyllakou, K., Kaltsonoudis, C., Nenes, A., and Pandis, S. N.: Rapid dark aging of biomass burning as an overlooked source of oxidized organic aerosol, P. Natl. Acad. Sci. USA, 117, 33028–33033, https://doi.org/10.1073/pnas.2010365117, 2020.

Kroll, J. H., Donahue, N. M., Jimenez, J. L., Kessler, S. H., Canagaratna, M. R., Wilson, K. R., Altieri, K. E., Mazzoleni, L. R., Wozniak, A. S., Bluhm, H., Mysak, E. R., Smith, J. D., Kolb, C. E., and Worsnop, D. R.: Carbon oxidation state as a metric for describing the chemistry of atmospheric organic aerosol, Nat. Chem., 3, 133–139, https://doi.org/10.1038/nchem.948, 2011.

Kuwata, M.: Atmospheric emissions, processes, and impacts of tropical peatland fire haze in Equatorial Asia: A review, Atmos. Environ., 331, 120575, https://doi.org/10.1016/j.atmosenv.2024.120575, 2024.

Kuwata, M., Kondo, Y., and Takegawa, N.: Critical condensed mass for activation of black carbon as cloud condensation nuclei in Tokyo, J. Geophys. Res.-Atmos., 114, D20202, https://doi.org/10.1029/2009JD012086, 2009.

Lau, H. C., Ramakrishna, S., Zhang, K., and Hameed, M. Z. S.: A Decarbonization Roadmap for Singapore and Its Energy Policy Implications, Energies, 14, 6455, https://doi.org/10.3390/en14206455, 2021.

Lee, J. H. and Hopke, P. K.: Apportioning sources of $PM_{2.5}$ in St. Louis, MO using speciation trends network data, Atmos. Environ., 40, 360–377, https://doi.org/10.1016/j.atmosenv.2005.11.074, 2006.

Lee, A. K. Y., Willis, M. D., Healy, R. M., Onasch, T. B., and Abbatt, J. P. D.: Mixing state of carbonaceous aerosol in an urban environment: single particle characterization using the soot particle aerosol mass spectrometer (SP-AMS), Atmos. Chem. Phys., 15, 1823–1841, https://doi.org/10.5194/acp-15-1823-2015, 2015.

Lee, A. K. Y., Willis, M. D., Healy, R. M., Wang, J. M., Jeong, C.-H., Wenger, J. C., Evans, G. J., and Abbatt, J. P. D.: Single-particle characterization of biomass burning organic aerosol (BBOA): evidence for non-uniform mixing of high molecular weight organics and potassium, Atmos. Chem. Phys., 16, 5561–5572, https://doi.org/10.5194/acp-16-5561-2016, 2016.

Lee, A. K. Y., Chen, C.-L., Liu, J., Price, D. J., Betha, R., Russell, L. M., Zhang, X., and Cappa, C. D.: Formation of secondary organic aerosol coating on black carbon particles near vehicular emissions, Atmos. Chem. Phys., 17, 15055–15067, https://doi.org/10.5194/acp-17-15055-2017, 2017.

Lee, A. K. Y., Rivellini, L. H., Chen, C. L., Liu, J., Price, D. J., Betha, R., Russell, L. M., Zhang, X., and Cappa, C. D.: Influences of Primary Emission and Secondary Coating Formation on the Particle Diversity and Mixing State of Black Carbon Particles, Environ. Sci. Technol., 53, 9429–9438, https://doi.org/10.1021/acs.est.9b03064, 2019.

Li, J., Pósfai, M., Hobbs, P. V., and Buseck, P. R.: Individual aerosol particles from biomass burning in southern Africa: 2, Compositions and aging of inorganic particles, J. Geophys. Res.-Atmos., 108, 8484, https://doi.org/10.1029/2002JD002310, 2003.

Li, W. J., Shao, L. Y., and Buseck, P. R.: Haze types in Beijing and the influence of agricultural biomass burning, Atmos. Chem. Phys., 10, 8119–8130, https://doi.org/10.5194/acp-10-8119-2010, 2010.

Lin, P., Aiona, P. K., Li, Y., Shiraiwa, M., Laskin, J., Nizkorodov, S. A., and Laskin, A.: Molecular Characterization of Brown Carbon in Biomass Burning Aerosol Particles, Environ. Sci. Technol., 50, 11815–11824, https://doi.org/10.1021/acs.est.6b03024, 2016.

Lin, P., Bluvshtein, N., Rudich, Y., Nizkorodov, S. A., Laskin, J., and Laskin, A.: Molecular Chemistry of Atmospheric Brown Carbon Inferred from a Nationwide Biomass Burning Event, Environ. Sci. Technol., 51, 11561–11570, https://doi.org/10.1021/acs.est.7b02276, 2017.

Liu, D., Whitehead, J., Alfarra, M. R., Reyes-Villegas, E., Spracklen, Dominick, V., Reddington, C. L., Kong, S., Williams, P. I., Ting, Y.-C., Haslett, S., Taylor, J. W., Flynn, M. J., Morgan, W. T., McFiggans, G., Coe, H., and Allan, J. D.: Black-carbon absorption enhancement in the atmosphere determined by particle mixing state, Nat. Geosci., 10, 184–188, https://doi.org/10.1038/ngeo2901, 2017.

Ma, M., Rivellini, L.-H., Cui, Y., Willis, M. D., Wilkie, R., Abbatt, J. P. D., Canagaratna, M. R., Wang, J., Ge, X., and Lee, A. K. Y.: Elemental analysis of oxygenated organic coating on black carbon particles using a soot-particle aerosol mass spectrometer, Atmos. Meas. Tech., 14, 2799–2812, https://doi.org/10.5194/amt-14-2799-2021, 2021.

Ma, M., Rivellini, L.-H., Kasthuriarachchi, N., Zhu, Q., Zong, Y., Yu, W., Yang, W., Kraft, M., and Lee, A. K. Y.: Effects of polyoxymethylene dimethyl ether (PODEn) blended fuel on diesel engine emission: Insight from soot-particle aerosol mass spectrometry and aethalometer measurements, Atmos. Environ. X, 18, 100216, https://doi.org/10.1016/j.aeaoa.2023.100216, 2023.

Malmborg, V. B., Eriksson, A. C., Shen, M., Nilsson, P., Gallo, Y., Waldheim, B., Martinsson, J., Andersson, O., and Pagels, J.: Evolution of In-Cylinder Diesel Engine Soot and Emission Characteristics Investigated with Online Aerosol Mass Spectrometry, Environ. Sci. Technol., 51, 1876–1885, https://doi.org/10.1021/acs.est.6b03391, 2017.

Massoli, P., Fortner, E. C., Canagaratna, M. R., Williams, L. R., Zhang, Q., Sun, Y., Schwab, J. J., Trimborn, A., Onasch, T. B., Demerjian, K. L., Kolb, C. E., Worsnop, D. R., and Jayne, J. T.: Pollution Gradients and Chemical Characterization of Particulate Matter from Vehicular Traffic near Major Roadways: Results from the 2009 Queens College Air Quality Study in NYC, Aerosol Sci. Tech., 46, 1201–1218, 10.1080/02786826.2012.701784, 2012.

Massoli, P., Onasch, T. B., Cappa, C. D., Nuamaan, I., Hakala, J., Hayden, K., Li, S.-M., Sueper, D. T., Bates, T. S., Quinn, P. K., Jayne, J. T., and Worsnop, D. R.: Characterization of black carbon-containing particles from soot particle aerosol mass spectrometer measurements on the R/V Atlantis during CalNex 2010, J. Geophys. Res.-Atmos., 120, 2575–2593, https://doi.org/10.1002/2014jd022834, 2015.

Murphy, D. M. and Thomson, D. S.: Chemical composition of single aerosol particles at Idaho Hill: Positive ion measurements, J. Geophys. Res.-Atmos., 102, 6341–6352, https://doi.org/10.1029/96JD00858, 1997.

Ng, N. L., Canagaratna, M. R., Zhang, Q., Jimenez, J. L., Tian, J., Ulbrich, I. M., Kroll, J. H., Docherty, K. S., Chhabra, P. S., Bahreini, R., Murphy, S. M., Seinfeld, J. H., Hildebrandt, L., Donahue, N. M., DeCarlo, P. F., Lanz, V. A., Prévôt, A. S. H., Dinar, E., Rudich, Y., and Worsnop, D. R.: Organic aerosol components observed in Northern Hemispheric datasets from Aerosol Mass Spectrometry, Atmos. Chem. Phys., 10, 4625–4641, https://doi.org/10.5194/acp-10-4625-2010, 2010.

Ng, N. L., Brown, S. S., Archibald, A. T., Atlas, E., Cohen, R. C., Crowley, J. N., Day, D. A., Donahue, N. M., Fry, J. L., Fuchs, H., Griffin, R. J., Guzman, M. I., Herrmann, H., Hodzic, A., Iinuma, Y., Jimenez, J. L., Kiendler-Scharr, A., Lee, B. H., Luecken, D. J., Mao, J., McLaren, R., Mutzel, A., Osthoff, H. D., Ouyang, B., Picquet-Varrault, B., Platt, U., Pye, H. O. T., Rudich, Y., Schwantes, R. H., Shiraiwa, M., Stutz, J., Thornton, J. A., Tilgner, A., Williams, B. J., and Zaveri, R. A.: Nitrate radicals and biogenic volatile organic compounds: oxidation, mechanisms, and organic aerosol, Atmos. Chem. Phys., 17, 2103–2162, https://doi.org/10.5194/acp-17-2103-2017, 2017.

Onasch, T. B., Trimborn, A., Fortner, E. C., Jayne, J. T., Kok, G. L., Williams, L. R., Davidovits, P., and Worsnop, D. R.: Soot Particle Aerosol Mass Spectrometer: Development, Validation, and Initial Application, Aerosol Sci. Tech., 46, 804–817, https://doi.org/10.1080/02786826.2012.663948, 2012.

Onasch, T. B., Fortner, E. C., Trimborn, A. M., Lambe, A. T., Tiwari, A. J., Marr, L. C., Corbin, J. C., Mensah, A. A., Williams, L. R., Davidovits, P., and Worsnop, D. R.: Investigations of SP-AMS Carbon Ion Distributions as a Function of Refractory Black Carbon Particle Type, Aerosol Sci. Tech., 49, 409–422, https://doi.org/10.1080/02786826.2015.1039959, 2015.

Othman, M., Latif, M. T., Hamid, H. H. A., Uning, R., Khumsaeng, T., Phairuang, W., Daud, Z., Idris, J., Sofwan, N. M., and Lung,

S.-C. C.: Spatial–temporal variability and health impact of particulate matter during a 2019–2020 biomass burning event in Southeast Asia, Sci. Rep., 12, 7630, https://doi.org/10.1038/s41598-022-11409-z, 2022.

Paatero, P. and Hopke, P. K.: Discarding or downweighting high-noise variables in factor analytic models, Anal. Chim. Acta, 490, 277–289, https://doi.org/10.1016/S0003-2670(02)01643-4, 2003.

Peng, J., Hu, M., Guo, S., Du, Z., Zheng, J., Shang, D., Levy Zamora, M., Zeng, L., Shao, M., Wu, Y. S., Zheng, J., Wang, Y., Glen, C. R., Collins, D. R., Molina, M. J., and Zhang, R.: Markedly enhanced absorption and direct radiative forcing of black carbon under polluted urban environments, P. Natl. Acad. Sci. USA, 113, 4266–4271, https://doi.org/10.1073/pnas.1602310113, 2016.

Petit, J. E., Favez, O., Albinet, A., and Canonaco, F.: A user-friendly tool for comprehensive evaluation of the geographical origins of atmospheric pollution: Wind and trajectory analyses, Environ. Model. Softw., 88, 183–187, https://doi.org/10.1016/j.envsoft.2016.11.022, 2017.

Polissar, A. V., Hopke, P. K., and Poirot, R. L.: Atmospheric Aerosol over Vermont: Chemical Composition and Sources, Environ. Sci. Technol., 35, 4604–4621, https://doi.org/10.1021/es0105865, 2001.

Reff, A., Eberly, S. I., and Bhave, P. V.: Receptor Modeling of Ambient Particulate Matter Data Using Positive Matrix Factorization: Review of Existing Methods, J. Air Waste Manag. Assoc., 57, 146–154, 2012.

Rivellini, L.-H., Adam, M. G., Kasthuriarachchi, N., and Lee, A. K. Y.: Characterization of carbonaceous aerosols in Singapore: insight from black carbon fragments and trace metal ions detected by a soot particle aerosol mass spectrometer, Atmos. Chem. Phys., 20, 5977–5993, https://doi.org/10.5194/acp-20-5977-2020, 2020.

Saarikoski, S., Timonen, H., Carbone, S., Kuuluvainen, H., Niemi, J. V., Kousa, A., Rönkkö, T., Worsnop, D., Hillamo, R., and Pirjola, L.: Investigating the chemical species in submicron particles emitted by city buses, Aerosol Sci. Tech., 51, 317–329, https://doi.org/10.1080/02786826.2016.1261992, 2016.

Saarikoski, S., Reyes, F., Vázquez, Y., Tagle, M., Timonen, H., Aurela, M., Carbone, S., Worsnop, D. R., Hillamo, R., and Oyola, P.: Characterization of submicron aerosol chemical composition and sources in the coastal area of Central Chile, Atmos. Environ., 199, 391–401, https://doi.org/10.1016/j.atmosenv.2018.11.040, 2019.

Sueper, D.: ToF-AMS Analysis Software, http://cires1.colorado.edu/jimenez-group/ToFAMSResources/ToFSoftware/ (last access: 18 June 2024), 2015.

Sun, Y. L., Zhang, Q., Schwab, J. J., Yang, T., Ng, N. L., and Demerjian, K. L.: Factor analysis of combined organic and inorganic aerosol mass spectra from high resolution aerosol mass spectrometer measurements, Atmos. Chem. Phys., 12, 8537–8551, https://doi.org/10.5194/acp-12-8537-2012, 2012.

Tehrani, M. W., Fortner, E. C., Robinson, E. S., Chiger, A. A., Sheu, R., Werden, B. S., Gigot, C., Yacovitch, T., Van Bramer, S., Burke, T., Koehler, K., Nachman, K. E., Rule, A. M., and DeCarlo, P. F.: Characterizing metals in particulate pollution in communities at the fenceline of heavy industry: combining mobile monitoring and size-resolved filter measurements, Environ. Sci.-Proc. Imp., 25, 1491–1504, https://doi.org/10.1039/D3EM00142C, 2023.

Ulbrich, I. M., Canagaratna, M. R., Zhang, Q., Worsnop, D. R., and Jimenez, J. L.: Interpretation of organic components from Positive Matrix Factorization of aerosol mass spectrometric data, Atmos. Chem. Phys., 9, 2891–2918, https://doi.org/10.5194/acp-9-2891-2009, 2009.

Van, D.-A., Vu, T. V., Nguyen, T.-H. T., Vo, L.-H. T., Le, N. H., Nguyen, P. H. T., Pongkiatkul, P., and Ly, B.-T.: A Review of Characteristics, Causes, and Formation Mechanisms of Haze in Southeast Asia, Curr. Pollut. Rep., 8, 201–220, https://doi.org/10.1007/s40726-022-00220-z, 2022.

Vasilakopoulou, C. N., Matrali, A., Skyllakou, K., Georgopoulou, M., Aktypis, A., Florou, K., Kaltsonoudis, C., Siouti, E., Kostenidou, E., Błaziak, A., Nenes, A., Papagiannis, S., Eleftheriadis, K., Patoulias, D., Kioutsioukis, I., and Pandis, S. N.: Rapid transformation of wildfire emissions to harmful background aerosol, npj Clim. Atmos. Sci., 6, 218, https://doi.org/10.1038/s41612-023-00544-7, 2023.

Wang, J., Onasch, T. B., Ge, X., Collier, S., Zhang, Q., Sun, Y., Yu, H., Chen, M., Prévôt, A. S. H., and Worsnop, D. R.: Observation of Fullerene Soot in Eastern China, Environ. Sci. Tech. Lett., 3, 121–126, https://doi.org/10.1021/acs.estlett.6b00044, 2016.

Wang, J., Zhang, Q., Chen, M., Collier, S., Zhou, S., Ge, X., Xu, J., Shi, J., Xie, C., Hu, J., Ge, S., Sun, Y., and Coe, H.: First Chemical Characterization of Refractory Black Carbon Aerosols and Associated Coatings over the Tibetan Plateau (4730 m a.s.l), Environ. Sci. Technol., 51, 14072–14082, https://doi.org/10.1021/acs.est.7b03973, 2017.

Wang, J., Ye, J., Liu, D., Wu, Y., Zhao, J., Xu, W., Xie, C., Shen, F., Zhang, J., Ohno, P. E., Qin, Y., Zhao, X., Martin, S. T., Lee, A. K. Y., Fu, P., Jacob, D. J., Zhang, Q., Sun, Y., Chen, M., and Ge, X.: Characterization of submicron organic particles in Beijing during summertime: comparison between SP-AMS and HR-AMS, Atmos. Chem. Phys., 20, 14091–14102, https://doi.org/10.5194/acp-20-14091-2020, 2020.

Wang, J., Ye, J., Zhang, Q., Zhao, J., Wu, Y., Li, J., Liu, D., Li, W., Zhang, Y., Wu, C., Xie, C., Qin, Y., Lei, Y., Huang, X., Guo, J., Liu, P., Fu, P., Li, Y., Lee, H. C., Choi, H., Zhang, J., Liao, H., Chen, M., Sun, Y., Ge, X., Martin, S. T., and Jacob, D. J.: Aqueous production of secondary organic aerosol from fossil-fuel emissions in winter Beijing haze, P. Natl. Acad. Sci. USA, 118, e2022179118, https://doi.org/10.1073/pnas.2022179118, 2021.

Willis, M. D., Lee, A. K. Y., Onasch, T. B., Fortner, E. C., Williams, L. R., Lambe, A. T., Worsnop, D. R., and Abbatt, J. P. D.: Collection efficiency of the soot-particle aerosol mass spectrometer (SP-AMS) for internally mixed particulate black carbon, Atmos. Meas. Tech., 7, 4507–4516, https://doi.org/10.5194/amt-7-4507-2014, 2014.

Willis, M. D., Healy, R. M., Riemer, N., West, M., Wang, J. M., Jeong, C.-H., Wenger, J. C., Evans, G. J., Abbatt, J. P. D., and Lee, A. K. Y.: Quantification of black carbon mixing state from traffic: implications for aerosol optical properties, Atmos. Chem. Phys., 16, 4693–4706, https://doi.org/10.5194/acp-16-4693-2016, 2016.

World Shipping Council: World Shipping Council: Top 50 world container ports, https://www.worldshipping.org/top-50-ports, last access: 25 April 2024.

Wu, Y., Cheng, T., Liu, D., Allan, J. D., Zheng, L., and Chen, H.: Light Absorption Enhancement of Black Carbon Aerosol Constrained by Particle Morphology, Environ. Sci. Technol., 52, 6912–6919, https://doi.org/10.1021/acs.est.8b00636, 2018.

Xu, J., Zhang, Q., Chen, M., Ge, X., Ren, J., and Qin, D.: Chemical composition, sources, and processes of urban aerosols during summertime in northwest China: insights from high-resolution aerosol mass spectrometry, Atmos. Chem. Phys., 14, 12593–12611, https://doi.org/10.5194/acp-14-12593-2014, 2014.

Xu, J., Zhang, Q., Shi, J., Ge, X., Xie, C., Wang, J., Kang, S., Zhang, R., and Wang, Y.: Chemical characteristics of submicron particles at the central Tibetan Plateau: insights from aerosol mass spectrometry, Atmos. Chem. Phys., 18, 427–443, https://doi.org/10.5194/acp-18-427-2018, 2018.

Xu, L., Suresh, S., Guo, H., Weber, R. J., and Ng, N. L.: Aerosol characterization over the southeastern United States using high-resolution aerosol mass spectrometry: spatial and seasonal variation of aerosol composition and sources with a focus on organic nitrates, Atmos. Chem. Phys., 15, 7307–7336, https://doi.org/10.5194/acp-15-7307-2015, 2015.

Yazdani, A., Takahama, S., Kodros, J. K., Paglione, M., Masiol, M., Squizzato, S., Florou, K., Kaltsonoudis, C., Jorga, S. D., Pandis, S. N., and Nenes, A.: Chemical evolution of primary and secondary biomass burning aerosols during daytime and nighttime, Atmos. Chem. Phys., 23, 7461–7477, https://doi.org/10.5194/acp-23-7461-2023, 2023.

Yu, C., Liu, D., Broda, K., Joshi, R., Olfert, J., Sun, Y., Fu, P., Coe, H., and Allan, J. D.: Characterising mass-resolved mixing state of black carbon in Beijing using a morphology-independent measurement method, Atmos. Chem. Phys., 20, 3645–3661, https://doi.org/10.5194/acp-20-3645-2020, 2020.

Zauscher, M. D., Wang, Y., Moore, M. J. K., Gaston, C. J., and Prather, K. A.: Air Quality Impact and Physicochemical Aging of Biomass Burning Aerosols during the 2007 San Diego Wildfires, Environ. Sci. Technol., 47, 7633–7643, https://doi.org/10.1021/es4004137, 2013.

Zhang, Q., Jimenez, J. L., Canagaratna, M. R., Allan, J. D., Coe, H., Ulbrich, I., Alfarra, M. R., Takami, A., Middlebrook, A. M., Sun, Y. L., Dzepina, K., Dunlea, E., Docherty, K., DeCarlo, P. F., Salcedo, D., Onasch, T., Jayne, J. T., Miyoshi, T., Shimono, A., Hatakeyama, S., Takegawa, N., Kondo, Y., Schneider, J., Drewnick, F., Borrmann, S., Weimer, S., Demerjian, K., Williams, P., Bower, K., Bahreini, R., Cottrell, L., Griffin, R. J., Rautiainen, J., Sun, J. Y., Zhang, Y. M., and Worsnop, D. R.: Ubiquity and dominance of oxygenated species in organic aerosols in anthropogenically-influenced Northern Hemisphere midlatitudes, Geophys. Res. Lett., 34, L13801, https://doi.org/10.1029/2007gl029979, 2007.

Zhang, Q., Jimenez, J. L., Canagaratna, M. R., Ulbrich, I. M., Ng, N. L., Worsnop, D. R., and Sun, Y.: Understanding atmospheric organic aerosols via factor analysis of aerosol mass spectrometry: a review, Anal. Bioanal. Chem., 401, 3045–3067, https://doi.org/10.1007/s00216-011-5355-y, 2011.

Zhang, Y., Wang, J., Cui, S., Huang, D. D., and Ge, X.: Aerosol Measurements by Soot Particle Aerosol Mass Spectrometer: a Review, Curr. Pollut. Rep., 6, 440–451, https://doi.org/10.1007/s40726-020-00162-4, 2020.